An experimental and detailed kinetic modeling study of the pyrolysis and oxidation of allene and propyne over a wide range of conditions

Combustion and Flame 233 (2021) 111578

Contents lists available at ScienceDirect

Combustion and Flame

journal homepage: www.elsevier.com/locate/combustflame

An experimental and detailed kinetic modeling study of the pyrolysis and oxidation of allene and propyne over a wide range of conditions

Snehasish Panigrahy[a,*], Jinhu Liang[a,b,**], Manik Kumer Ghosh[a], Quan-De Wang[a,c], Zhaohong Zuo[a,d], Shashank Nagaraja[a], A. Abd El-Sabor Mohamed[a], Gihun Kim[e], Subith S. Vasu[e], Henry J. Curran[a]

[a] Combustion Chemistry Center, School of Chemistry, MaREI Center, Ryan Institute, NUI Galway, Ireland
[b] School of environmental and safety engineering, North University of China, Taiyuan 030051, PR China
[c] Low Carbon Energy Institute, China University of Mining and Technology, Xuzhou 221008, PR China
[d] School of chemistry and chemical engineering, Chongqing University, Chongqing 401331, PR China
[e] Center for Advanced Turbomachinery and Energy Research (CATER), Mechanical and Aerospace Engineering, University of Central Florida, Orlando, FL 32816, USA

ARTICLE INFO

Article history:
Received 20 February 2021
Revised 21 June 2021
Accepted 22 June 2021

Keywords:
Allene
Propyne
Ignition delay time
Pyrolysis
Laminar flame speed
Kinetic modeling

ABSTRACT

Allene and propyne are important intermediates in the pyrolysis and oxidation of higher hydrocarbon fuels, and they are also a major source of propargyl radical formation, which can recombine into different C_6H_6 isomers and finally produce soot. In a prior work (Panigrahy et al., "A comprehensive experimental and improved kinetic modeling study on the pyrolysis and oxidation of propyne", Proc. Combust. Inst 38 (2021)), the pyrolysis, ignition , and laminar flame speed of propyne were investigated. To understand the kinetic features of initial fuel breakdown and oxidation of the two C_3H_4 isomers, new measurements for allene pyrolysis and oxidation are conducted in the present paper at the same operating conditions as those studied previously for propyne. Ignition delay times of allene are measured using a high-pressure shock tube and a heated twin-opposed piston rapid compression machine in the temperature range 690–1450 K at equivalence ratios of 0.5, 1.0 and 2.0 in 'air', and at pressures of 10 and 30 bar. Pyrolysis species measurements of allene and propyne are also performed using a gas chromatography integrated single-pulse shock tube in the temperature range 1000–1700 K at pressure of 2 and 5 bar. Furthermore, laminar flame speeds of allene are measured at elevated gas temperatures of 373 K at pressures of 1 and 2 bar for a wide range of equivalence ratios from 0.6 to 1.5. A newly updated kinetic mechanism developed for this study is the first model that can well reproduce all of the experimental results for both allene and propyne. It is observed that in the pyrolysis process, allene dissociates faster than propyne. Both isomers exhibit similar ignition delay times at high temperatures (>1000 K), while, at intermediate temperatures (770–1000 K) propyne is the faster to ignite, and at lower temperatures (< 770 K) allene becomes more reactive. Furthermore, laminar flame speeds for propyne are found to be slightly faster than those for allene under the conditions studied in this work.

1. Introduction

Allene (C_3H_4-a) and propyne (C_3H_4-p) are two crucial intermediates produced in the decomposition and oxidation of higher hydrocarbon fuels, such as propane [1], propene [2] and heavier hydrocarbons [3] including kerosene [4]. Moreover, they are also a major source of propargyl ($\dot{C}_3H_3$) radical formation, which can recombine into different C_6H_6 isomers [5]. These recombination reactions are believed to be the dominant benzene (C_6H_6) production pathways in the pyrolysis and oxidation of organic fuels [6,7]. As the first aromatic ring, C_6H_6 is considered to be the main precursor leading to the generation of polycyclic aromatic hydrocarbons (PAHs) [8], and PAHs are the precursors of particulate and soot [9,10]. Therefore, an accurate understanding of the combustion mechanism of C_3H_4-a and C_3H_4-p is key to the devel-

* Corresponding author.
** Corresponding author at: Combustion Chemistry Center, School of Chemistry, MaREI Center, Ryan Institute, NUI Galway, Ireland.
E-mail addresses: snehasish.panigrahy@nuigalway.ie (S. Panigrahy), jhliang@nuc.edu.cn (J. Liang).

https://doi.org/10.1016/j.combustflame.2021.111578

Table 1
Experimental literature data for C_3H_4-a oxidation and pyrolysis.

No.	Fuel	Reactor	φ	Dilution (%)	T (K)	p (atm)	Reference	Year
1	C_3H_4-a/-p	ST/JSR	0.5–2.0	97–98 (Ar)	800–2030	1.0–10.0	Curran et al. [11]	1996
2	C_3H_4-a/-p	ST	0.5, 1.0	85–95(Ar)	1200 – 1680	0.3–4.0	Fournet et al. [12]	1999
3	C_3H_4-a/-p	ST	∞	98–99.75 (Ar)	1040 – 1470	1.2–6.0	Lifshitz et al. [13]	1976
4	C_3H_4-a/-p	ST	∞	99.85 (Ar)	1300 – 2100	–	Kakumoto et al. [14]	1987
5	C_3H_4-a	ST	∞	95.7 (Ne)	1300 – 2000	0.2–0.5	Wu et al. [15]	1987
6	C_3H_4-a/-p	ST	∞	96–99 (Ar)	1200 – 1570	1.7–2.6	Hidaka Y.et al. [16]	1989
7	C_3H_4-a/-p	ST	∞	96–98 (Ne)	1770 – 2500	0.13–0.86	Kiefer et al. [17]	1997
8	H_2 + C_3H_4-a	Flat flame burner	1.5	61.5, 62.5 (Ar)	400–1100	0.033	Pauwels et al. [18]	1995
9	C_2H_2 + C_3H_4-a/-p	Flat flame burner	1.67	56.5, 60.7 (Ar)	600–2200	0.033	Miller et al. [19]	1996
10	C_2H_4 + C_3H_4-a/-p	Flat flame burner	0.7	56.4, 56.5 (Ar)	300–2400	0.04	Law et al. [20]	2005
11	CH_4 + C_3H_4-a/-p	Flat flame burner	1.25, 1.55	43.2, 45.7 (Ar)	600–2000	0.067	Gueniche et al. [21]	2006
12	C_3H_4-a/-p	Flat flame burner	1.8	40.8 (Ar)	1300–2300	0.033	Hansen et al. [22]	2007
13	C_3H_4-a/-p	Flat flame burner	1.0	44.4 (Ar)	400–2200	0.033	Hansen et al. [23]	2009
14	C_3H_4-a	JSR	0.2–2.0	97 – 99 (N_2)	1030–1070	1.0	Dagaut et al. [24]	1990
15	C_3H_4-a/-p	JSR	0.2–2.0	99.2 (N_2)	800–1200	1.0–10.0	Faravelli et al. [9]	2000

opment of hierarchical hydrocarbon chemistry models, particularly for PAHs and soot formation.

A considerable number of experimental and kinetic modeling investigations of the two C_3H_4 isomers are available in the literature [11]–[24], specifically at low-pressure and high-temperature conditions. Table 1 summarizes these previous studies and includes the types of reactors and experimental conditions. These include shock tube ignition delay time (IDT) measurements [11,12], pyrolysis studies using shock tubes (ST) [13]–[17], laminar flame speed (LFS) measurements using flame burners [18]–[23], and products species concentration profiles obtained using a jet-stirred reactor (JSR) and a flow reactor [9,24].

The first C_3H_4-a IDT measurements were published by Curran et al. [11]. A single-pulse shock was utilized to investigate C_3H_4-a and C_3H_4-p ignition characteristics in the pressure (p_C) range of 2–5 atm in the temperature range 1200–1900 K, and at equivalence ratios of 0.5, 1.0, and 2.0 diluted in Ar. A detailed high-temperature mechanism describing the oxidation of C_3H_4-a and C_3H_4-p was developed. The IDT results showed that both isomers exhibit similar ignition characteristics at these high temperatures. The most recent C_3H_4-a IDT measurements were published by Fournet et al. [12]. The objective of their work was to investigate the oxidation of C_3H_4-p, C_3H_4-a, and acetylene (C_2H_2) and build a detailed mechanism. IDT measurements were conducted in a shock tube in the temperature range 1200–1680 K, at low pressures (0.3–4.0 atm) for equivalence ratios of 0.5 and 1.0.

A variety of C_3H_4-a shock tube pyrolysis experiments were performed by Lifshitz et al. [13], Kakumoto et al. [14], Wu et al. [15], Hidaka et al. [16], and Kiefer et al. [17]. The first decomposition and isomerization experiments were examined by Lifshitz et al. [13] in the temperature range 1040–1470 K at pressures in the range 1.2–6.0 atm in a single pulse shock tube (SPST) using gas chromatography (GC) to detect species concentrations. Kakumoto et al. [14] investigated the inter-isomerization of C_3H_4-a and C_3H_4-p in the temperature range 1300–2100 K using IR emission to monitor the isomerization rate. They found the process occurred in the fall-off region via a series of successive reactions involving cyclopropane. Subsequently, low pressure (0.2–0.5 atm) shock tube pyrolysis experiments of 4.3% C_3H_4-a/Ne mixtures were performed by Wu and Kern [15] in the temperature range 1300–2000 K. Moreover, a model was developed by including the initial step of C–H scission for both of the C_3H_4 isomers as well as an isomerization reaction and the formation of cyclic compounds from linear unsaturated hydrocarbons. Subsequently, Hidaka et al. [16] utilized a shock tube to investigate the thermal decomposition of highly diluted C_3H_4-a/Ar and C_3H_4-p/Ar mixtures in the temperature and pressure ranges of 1200–1570 K and 1.7–2.6 atm, respectively. C_3H_4-a and C_3H_4-p time history profiles were recorded using IR emission at 3.48 μm and/or 5.18 μm for these pyrolysis experiments. Reactant and product species concentration profiles were also measured using a GC with a flame ionization detector (FID).

Most C_3H_4-a LFS studies have centered on doped flames. The main aim of these works was to understand the combustion chemistry of $\dot{C}_3H_3$ radicals and other related species (including C_3H_4-a and C_3H_4-p) in flame conditions by adding C_3H_4-a to other fuels including hydrogen (H_2) [18], C_2H_2 [19], ethylene (C_2H_4) [20] and methane (CH_4) [21]. A flat-flame burner with different analytical methods (mass spectrometry, laser-induced fluorescence (LIF) and gas chromatography-mass spectrometry (GC–MS) were used to perform these experiments at various conditions (see Table 1, numbers 18–23). With the development of combustion diagnostic technologies, flame-sampling photoionization molecular beam mass spectrometry with tuneable vacuum-ultraviolent synchrotron radiation was used to measure the mole fraction profiles of different flame species to clarify the isomer-specific reaction mechanism in C_3H_4-a and C_3H_4-p flames [22,23]. Dagaut et al. [24] experimentally assessed the concentrations profiles of major species produced from the oxidation of C_3H_4-a in a JSR at atmospheric pressure over the temperature range 1030–1070 K.

Faravelli et al. [9] conducted an oxidation study of C_3H_4-p and C_3H_4-a in a JSR at pressures in the range 1–10 atm, at temperatures in the range 800–1200 K. A semi-detailed kinetic model involving approximately 100 species and 1500 reactions was developed for intermediate and high temperatures and validated using their JSR and shock tube data. It is observed from the literature that all IDT experiments for C_3H_4-a were measured in STs at relatively low pressures (0.3–10 atm) and at high-temperature conditions (1200–1900 K). There is a lack of IDTs data available for C_3H_4-a at low to intermediate temperatures ($<$ 1100 K) and at high pressures ($\geq$ 10 bar). Moreover, there are only a few studies available for high temperature C_3H_4-a oxidation, mostly focusing on doped flames. Therefore, additional experimental IDT data at engine-relevant conditions for higher pressures and lower temperatures are needed to study the chemical kinetics of C_3H_4-a ignition characteristics. Furthermore, LFS measurements are also needed to obtain a better understanding of C_3H_4-a flame speeds at high-temperature conditions.

In the current study, new IDTs of C_3H_4-a are measured using a high-pressure shock tube (HPST) and a rapid compression machine (RCM) at equivalence ratios of 0.5, 1.0, and 2.0 in 'air', at 10 and 30 bar pressures over the temperature range of 690 – 1450 K. In addition, the pyrolysis of C_3H_4-a has also been investigated at pressures of 2 and 5 bar in the temperature range 1000 – 1700 K in two different SPSTs to measure the concentration profiles of the stable species products using a GC integrated with FID and ther-

Table 2
Molar composition of C_3H_4-a IDT experiments.

C_3H_4-a	O_2	Diluent	φ	p_C (bar)
2.56	20.46	76.98	0.5	10, 30
4.99	19.95	75.06	1.0	10, 30
9.50	19.00	71.50	2.0	10, 30
Molar composition of pyrolysis mixtures				
C_3H_4-a/C_3H_4-p	Diluent	Internal standard gas (Kr)	p_C (bar)	
2.0	97.5	0.5	5	

mal conductivity detectors. The LFSs of C_3H_4-a/'air' are also studied at an elevated gas temperature of 373 K and at two different pressures (1 and 2 bar) for a wide range of equivalence ratios (0.6–1.5). An added objective of the current paper is to distinguish the kinetic features of early fuel breakdown and oxidation of the two C_3H_4 isomers by comparing and contrasting the new measurements for IDTs, pyrolysis and LFS of C_3H_4-a to our recently published data for C_3H_4-p [25] at identical conditions of temperature, pressure and mixture composition. A newly developed and improved detailed kinetic mechanism based on NUIGMech1.1 [25] is used to describe the pyrolysis as well as the low- and high-temperature oxidation behavior of the two C_3H_4 isomers.

2. Experimental methods

IDT measurements of C_3H_4-a oxidation were conducted in a HPST and in a twin-opposed piston RCM at NUI Galway (NUIG). The pyrolysis experiments were carried out using two different SPSTs at the North University of China (NUC) and at NUIG [25]. The flame speed measurements were conducted in a spherical vessel at the University of Central Florida (UCF) for an unburned C_3H_4-a/'air' mixture temperature of T_U = 373 K, at pressures (p_C) of 1 and 2 bar. Table 2 provides a summary of the experimental IDT and pyrolysis conditions studied here. For the experiments performed at NUIG, C_3H_4-a was acquired from Air Liquide at 97% purity. O_2, N_2 and Ar were acquired from BOC Ireland at high purity (≥ 99.5%). For the experiments performed at NUC, C_3H_4-a and C_3H_4-p were acquired from Jinhan gas Ltd., China at 97% purity. Krypton (99.99%) was also obtained from Jinhan gas Ltd., China, and was utilized as an internal standard gas in the pyrolysis experiments. The purity of C_3H_4-a provided by the supplier was examined using gas chromatography, and the presence of 3% C_3H_4-p was detected in the GC chromatogram. The effects on the predictions of IDTs and flame speeds of the addition of 3% C_3H_4-p to a pure C_3H_4-a/'air' mixture are shown in the Fig. S1. The simulation results confirm that there is no significant effect of the impurity on predicted IDTs and on the flame behavior of C_3H_4-a/'air' mixtures. For the LFS measurements performed at UCF, C_3H_4-a was supplied by Synquest Laboratories (> 97%), Oxygen and nitrogen were supplies by NexAir at high purity (> 99.999%).

2.1. NUI Galway high pressure shock tube

The IDT measurements of the C_3H_4-a/'air' mixtures were performed in the HPST at NUIG at equivalence ratios of 0.5, 1.0 and 2.0, at pressures of 10 and 30 bar and in the temperature range 900–1450 K. The detailed features of the ST setup were described previously [26,27]–[28]. Briefly, the shock tube has a 5.7 m driven section, a 3.0 m long driver section, and the double diaphragm linking the driver and the driven segment is 0.03 m long with an inner diameter of 63.5 mm. The velocity of the incident shock wave was measured uisng six PCB 113B24 piezoelectric pressure transducers located in the sidewall of the driven section. A Kistler 603CAB piezoelectric pressure transducer located in the endwall of the driven section, connected to a Kistler 5018 charge amplifier, is used to measure the pressure-time histories. All pressure traces are monitored using two digital TiePie Handyscope HS4 oscilloscopes. The pressure and temperature behind the reflected shock wave are determined from the reflected shock routine in Gaseq [29]. A detailed description of how the post-shock conditions are calculated was provided in a previous study [30]. The uncertainty in reflected shock temperature is calculated to be less than ± 20 K, which can give rise to a 20% uncertainty in the measured IDTs, τ_{ign} [28]. The IDT is defined as the time period between the increase in pressure caused by the arrival of the incident shock at the endwall and the maximum rate of increase of the pressure signal, as shown in Fig. 1.

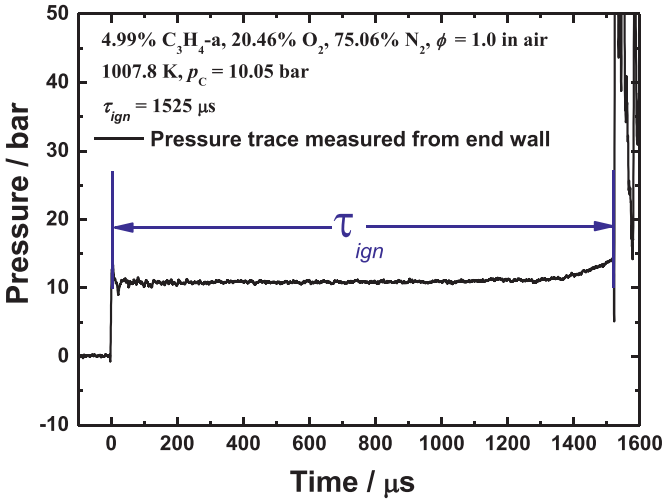

Fig. 1. A typical pressure trace for C_3H_4-a oxidation in the NUIG-HPST.

2.2. NUI Galway rapid compression machine

The low to intermediate temperature range IDT studies (690–880 K) of the C_3H_4-a/'air' mixtures were conducted in the opposed twin-piston red RCM configuration at NUIG at equivalence ratios of 0.5, 1.0 and 2.0, and at the pressures of 10 and 30 bar. The details of the RCM can be found in [31,32]–[33], and only a brief description is given here.

The opposed twin-piston contains two creviced piston heads with an inner diameter of 38.2 mm, which greatly aids temperature homogeneity throughout the combustion chamber after compression [34]. The opposed twin-piston configuration here leads to a short compression time of 16 ms, while the compression ratio of this facility is approximately 10. Since the compression ratio does not vary, the required compressed gas pressures and temperatures are obtained by varying the initial pressure, initial temperature, and the inert gas compositions (Ar and N_2). Five thermocouples are mounted on the wall of the combustion chamber and on the sleeves. A Kistler 6045B piezoelectric pressure transducer placed flush to the wall of the combustion chamber was used to record the pressure-time history, which was stored using a digital oscilloscope (PicoScope 5000 series). The compressed gas temperature was determined using the adiabatic/compression expansion routine in Gaseq [29], assuming frozen chemistry. The IDT was determined as the time period between the first local maximum pressures to the increase in the maximum rate of the pressure trace caused by the ignition, Fig. 2. The reactive pressure traces 1 and 2 shown in Fig. 2 demonstrate the good repeatability and reproducibility of our measurements from two similar experiments. Non-reactive pressure traces required for the simulations are obtained by replacing O_2 with N_2 in the oxidizer. To model the effect

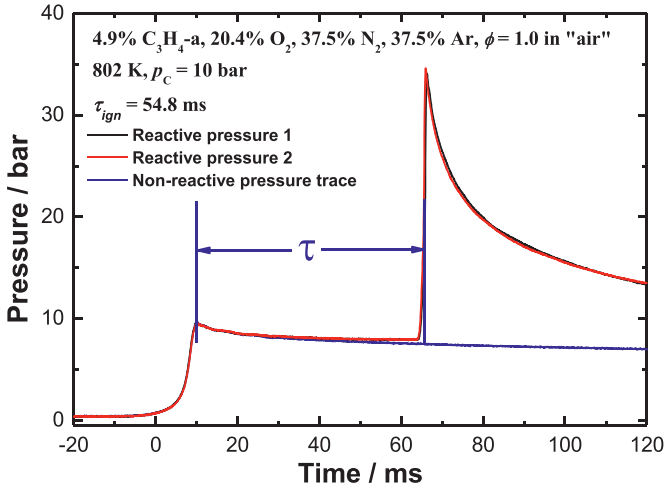

Fig. 2. A typical pressure trace for C_3H_4-a oxidation in the NUIG RCM.

of heat loss during compression, the pressure traces are converted to volume-time profiles, which are to be applied in the kinetic simulations. The largest uncertainty of compressed temperature was estimated to be less than 15 K, and the largest uncertainty in IDTs is estimated to be less than 5%.

2.3. NUC single-pulse shock tube

The pyrolysis experiments for the C_3H_4-a/Ar and C_3H_4-p/Ar mixtures were performed at NUC in a SPST at 5 bar in the temperature range 1000 – 1700 K, for reaction times in the range 1.46–1.83 ms using a GC to measure mole fractions of the major intermediate and product species. The detailed description of the SPST is as follows. It is composed of a 1.5 m driver section and a 3.05 m driven section, with an inner diameter of 44 mm. The driver and driven sections are isolated using a polycarbonate diaphragm. The dump tank is connected near the diaphragm section of the driven tube by a manually operated ball valve with a diameter of 44 mm. The dump tank is a pressure vessel that can consume the reflected shock wave, ensuring that the reaction mixture only undergoes a single heated condition. The dump tank is linked to an Inficon PSG500 Pirani gauge and an Inficon CDG100 (1000 Torr) capacitance gauge and has connections for its evacuation and for the supply of argon. The experimental procedure and product analysis method are almost the same as described by Nagaraja et al. [25] and will only be briefly described here. Before each experiment, the ball valve to the dump tank is closed. The dump tank and driven section is evacuated to 5×10^{-2} Pa using a rotary pump and a turbo molecular pump and the pressure is monitored using a MKS 901P Pirani gauge. Once the ultimate vacuum is attained, the driven section is filled with the reactants to the desired pressure, which is regulated by the Inficon CDG 100 capacitance manometer. The normal shock equation of Gaseq program [29] is utilized to calculate this pressure. The velocity of the shock wave is measured using four PCB 113B21 and one piezoelectric pressure transducers located in the sidewall and endwall of the driven section, respectively. The Kistler transducer is also employed to record the pressure-time profiles .

The shock heated products are collected from the endwall using a solenoid valve with a 3 mm inner diameter tube that protrudes 10 mm into the ST and are analysed using a GC (Agilent 7820A). An FID and a TCD are used to analyze the reaction products. Kr is used as an internal standard for all measurements. The concentrations of the species with no calibration standard are estimated using the effective carbon number concept. The uncertainties in the measured temperatures behind the reflected shock caused by shock velocities are found to be ± 2%. The experimental uncertainty of the calibrated species mole fractions determined using repetitive sampling of the standard gas is estimated as ± 10%. For reactant mole fractions the uncertainty is approximately ± 0.02%. The uncertainty in the reactant mole fraction is based on the mixture preparation using the available pressure gauges. A mixture is prepared to 1000 Torr based on the partial pressures of the components with an accuracy of ± 0.2 Torr. Therefore, the uncertainty in the reactant mole fraction is ± 0.02%. The uncertainty is approximately ± 5% for the residence time. The carbon balances from the GC measurements are 100 ± 15%. The uncertainties in the properties from experimental procedures are generally consistent with other similar facilities [25]. We were unable to detect species > C_6, because the detection limit of the GC was not low enough to detect the formation of these higher hydrocarbons in very small amounts. It is difficult to identify and quantify aromatic species due to the limitations of the experimental set-up.

2.4. Laminar flame speed measurements

Flame speed measurements of C_3H_4-a/'air' mixtures were obtained using the spherical vessel setup at UCF. The mixture preparation system of the experimental setup consisted of the mixing tank for producing synthetic air from reactant tanks, a rotary vane vacuum pump, and a liquid fuel injection port. More details of this facility were presented previously [35,36]–[37]. The MKS 628F Baratron and MKS E27 Baratron manometers are used to measure accuracy at high-range (0.2–20,000 Torr) and low-range (0.001–100 Torr) pressures, respectively. A furnace inside the spherical vessel controls the temperature of the combustion chamber, and *K*-type thermocouples are used to monitor its temperature. A high-speed camera (Phantom v12.1) is used to capture the flame propagation data inside the combustion chamber. Mixtures of research grade C_3H_4-a and artificial air were supplied inside the vessel applying the partial pressure concept, which was recorded by utilizing two Baratron gauges. C_3H_4-a was supplied first at an elevated temperature of 373 K. To warrant homogeneity of the synthetic air, oxygen/nitrogen mixtures in a ratio of 1/3.76 are mixed for 2 h before performing the experiments. A National Instruments DAQ (PCI-6259) system is used to record the data. A waiting time of 5 min for mixture homogeneity was applied before it is ignited by a spark. The constant volume method is applied to calculate laminar flame speeds using a multizone model. Details are in [35]–[37], with a brief explanation provided here. The multizone model consists of two zones: burned and unburned. Equilibrium calculation was used to obtain the properties of each burned zone during combustion. After calculating the properties of the burned gases, the flame speed was calculated from the measured pressure time-histories. The flame stretch rate effect is an important parameter to calculate laminar flame speed measurement in a constant-volume chamber. However, the stretch effect is not considered in this study because the stretch effects approach zero with the increasing radius of a flame [38,39]. The average uncertainty in measured laminar flame speed was approximately 5.9%.

3. Kinetic modeling and simulation methods

The detailed kinetic mechanism used in this study is developed based on the recently published NUIGMech1.1 [25] model which was hierarchically developed and widely validated for the combustion of C_1 – C_7 hydrocarbons. In our previous work [25], the C_3H_4-p sub-chemistry was published as a part of the overall NUIGMech1.1 model development, and is retained in the present mechanism. The C_3H_4-a sub-mechanism in the model presented here,

Table 3
Rate coefficients of the important reactions updated in NUIGMech1.2 and not present in AramcoMech3.0, $k = AT^n exp\ (E_0/RT)$, where R = 1.987 cal K^{-11} mol^{-1}. The units are cm^3, moles, seconds, and Kelvin.

Reaction	A	n	E_0	Ref.
$\dot{C}_3H_3 + \dot{H} \leftrightarrow C_3H_4$-p	7.943E + 29	−5.06	4861.	[43][a]
$\dot{C}_3H_3 + \dot{H} \leftrightarrow C_3H_4$-a	3.162E + 29	−5.00	4711.	[43][a]
C_3H_4-a + $\dot{H} \leftrightarrow C_2H_2 + \dot{C}H_3$	6.625E + 03	3.095	5522.	[48]
C_3H_4-p + $\dot{H} \leftrightarrow C_2H_2 + \dot{C}H_3$	2.86E + 04	2.825	4821.	[48]
C_3H_4-a + $\dot{O}H \leftrightarrow \dot{C}_3H_3 + H_2O$	5.05E + 05	2.36	2879.	[49][c]
	5.95E + 04	2.5	661.1	
C_3H_4-p + $\dot{O}H \leftrightarrow \dot{C}_3H_3 + H_2O$	3.87E + 05	2.34	2173.	[49][c]
	4.93E + 04	2.48	62.	
C_3H_4-a + $\ddot{O} \leftrightarrow \dot{C}_3H_3O + \dot{H}$	3.85E + 06	2.05	180.	[50][b, d]
C_3H_4-a + $\ddot{O} \leftrightarrow \dot{C}H_2 + CH_2CO$	3.85E + 06	2.05	180.	[50][b, d]
C_3H_4-a + $\ddot{O} \leftrightarrow \dot{C}_3H_3 + \dot{O}H$	1.93E + 06	2.05	180.	[50][b, d]
C_3H_4-p + $\ddot{O} \leftrightarrow \dot{C}_3H_3 + \dot{O}H$	7.58E + 01	0.048	3550.	[51][a]
C_3H_4-p + $\ddot{O} \leftrightarrow \dot{C}_2H_3 + H\dot{C}O$	2.4E + 12	−0.012	1950.	[51][a]
C_3H_4-p + $\ddot{O} \leftrightarrow C_2H_4 + CO$	2.95E + 14	−0.587	2220.	[51][a]
C_3H_4-p + $\ddot{O} \leftrightarrow C_2H_2 + CO + H_2$	8.45E + 22	−3.54	5020.	[51][a, d]
C_3H_4-p + $\ddot{O} \leftrightarrow \dot{C}H_3 + H\dot{C}CO$	1.20E + 10	0.901	2170.	[51][a]
C_3H_4-p + $\ddot{O} \leftrightarrow CH_3\dot{C}CO + \dot{H}$	1.9E + 10	0.803	2850.	[51][a, d]
C_3H_4-p + $\ddot{O} \leftrightarrow \dot{C}_3H_3O + \dot{H}$	1.9E + 06	1.89	2740.	[51][a, d]
C_3H_4-p + $\ddot{O} \leftrightarrow C_2H_3\dot{C}O + \dot{H}$	5.1E + 04	2.16	2340.	[51][a, d]
C_3H_4-p + $\dot{O}H \leftrightarrow p\dot{C}_3H_4OH$-2	5.36E + 47	−10.93	14,280.	[49][a, c]
	3.15E + 33	−7.11	5101.	
C_3H_4-p + $\dot{O}H \leftrightarrow CH_3C(OH)\dot{C}H$	5.38E + 45	−10.36	1481.	[49][a, c]
	3.81E + 29	−5.96	4629.	
C_3H_4-p + $\dot{O}H \leftrightarrow CH_2CO + \dot{C}H_3$	4.07E + 26	−4.29	12,560.	[49][a, c, d]
	4.68E + 06	1.6	3216.	
C_3H_4-a + $\dot{O}H \leftrightarrow S\dot{C}_3H_4OH$	8.67E + 22	−3.1	5518.	[49][a, c]
	5.79E - 28	10.4	−22,290.	
C_3H_4-a + $\dot{O}H \leftrightarrow CH_2\dot{C}CH_2OH$	2.59E + 44	−9.87	12,970.	[49][a, c]
	4.77E + 29	−5.88	3477.	
C_3H_4-a + $\dot{O}H \leftrightarrow CH_2CO + \dot{C}H_3$	1.51E+04	2.2	1759.	[49][a, c, d]
	4.47E + 20	−1.9	20,040.	
C_3H_4-a + $H\dot{O}_2 \leftrightarrow CH_2COOH\dot{C}H_2$	3.3E + 28	−5.41	19,090.	a. b, d
C_3H_4-a + $H\dot{O}_2 \leftrightarrow CH_2CO\dot{O}CH_3$	6.85E + 20	−4.145	9146.	a. b, d
C_3H_4-a + $H\dot{O}_2 \leftrightarrow \dot{C}H_2CO\dot{C}H_2 + \dot{O}H$	2.37E + 09	0.896	18,121.	a. b, d
C_3H_4-a + $H\dot{O}_2 \leftrightarrow CH_3CO\dot{C}H_2 + \ddot{O}$	1.000E + 00	3.476	13,133.	a. b, d
C_3H_4-a + $H\dot{O}_2 \leftrightarrow \dot{C}H_3CO\dot{C}H + \dot{O}H$	1.000E + 00	2.956	14,163.	a. b, d
C_3H_4-a + $H\dot{O}_2 \leftrightarrow CH_2O + \dot{C}H_3CO$	1.000E+00	2.956	6028.	a. b, d
C_3H_4-a + $H\dot{O}_2 \leftrightarrow C_3H_4$-*p* + $H\dot{O}_2$	1.000E + 00	3.090	15,594.	a. b, d
C_3H_4-a + $H\dot{O}_2 \leftrightarrow \dot{C}H_3O$+$CH_2CO$	1.000E + 00	2.274	8329.	a. b, d
$CH_2COOH\dot{C}H_2 \leftrightarrow \dot{C}H_2CO\dot{C}H_2 + \dot{O}H$	1.000E + 00	3.389	19,558.	a. b, d
$CH_2\dot{C}CH_2OOH \leftrightarrow C_3H_4$-a + $H\dot{O}_2$	2.72E + 14	−0.381	18,200.	[62][d]
$CH_2\dot{C}CH_2OH + O_2 \leftrightarrow CH_2C(O\dot{O})CH_2OH$	5.52E + 42	−9.87	8633.	[42][a, d]
C_3H_4-p + $H\dot{O}_2 \leftrightarrow CH_3\dot{C}CHO + \dot{O}H$	1.56E + 10	0.77	19,000.	[52][a, c, d]
	2.50E + 07	1.56	14,790.	
C_3H_4-p + $H\dot{O}_2 \leftrightarrow CH_3CHC\dot{H}O + \ddot{O}$	1.98E + 74	−16.33	109,200.	[52][a, c, d]
	6.57E + 04	1.85	12,360.	
C_3H_4-p + $H\dot{O}_2 \leftrightarrow CH_2O + \dot{C}H_3CO$	8.07E + 07	0.6	10,850.	[52][a, c, d]
	3.33E + 102	−24.	138,600.	
$\dot{C}_3H_3 \leftrightarrow C_3H_2C + \dot{H}$	1.33E + 03	−4.87	93,410.	[53][d]
$\dot{C}_3H_3 \leftrightarrow \dot{C}_3H_2 + \dot{H}$	6.46E + 40	−7.55	108,900.	[53][d]
$\dot{C}_3H_3 + \dot{O}H \leftrightarrow \dot{C}_2H_3 + H\dot{C}O$	1.095E + 19	−1.65	4628.	[54]
$\dot{C}_3H_3 + \dot{O}H \rightarrow H_2 + C_2H_2 + CO$	1.51E + 20	−2.2	3992.	[54]
$\dot{C}_3H_2 + O_2 \leftrightarrow H\dot{C}CO + CO + \dot{H}$	2.50E + 05	2.245	367.6	[55][d]
$\dot{C}_3H_2 + \dot{O}H \leftrightarrow C_2H_2 + \dot{H} + CO$	3.53E + 22	−2.4	14,682.7	[55][d]

[a] The rate coefficients are for 1 atm pressure.
[b] See text for detail.
[c] Declared as duplicate reactions.
[d] Reactions were absent in AramcoMech3.0.

NUIGMech1.2, is developed to match the new experimental data from the current work and is included as Supplementary material.

Table 3 summarizes the rate coefficients of the important and additional reactions updated in NUIGMech1.2 compared to AramcoMech3.0 [40]. The thermodynamic parameters in NUIGMech1.2 are obtained primarily from the Burcat database [41]. Where possible, both the reaction rate coefficients and thermochemical properties associated with the C_3H_4-a and C_3H_4-p sub-mechanism are taken from recent quantum chemistry studies. For example, the thermodynamic properties of all species on the $C_3H_5O_2$ and C_3H_4 potential energy surfaces are adopted from the theoretical studies by Chen et al. [42] and Miller et al. [43], respectively. In the absence of data in the literature, group additivity was used to calculate the thermodynamic properties for all of the other species. NUIGMech1.2 has been extensively validated against the available experimental data for C_3H_4-a and C_3H_4-p. Comparisons of the model to jet-stirred reactor [44], flow reactor [45], fuel-rich flat flame burner species profiles from Hansen et al. [46] and shock tube IDTs data from Curran et al. [11] for the oxidation of both C_3H_4-a and C_3H_4-p are provided as Supplementary material.

All of the simulations are performed using CHEMKIN-Pro [] with different codes. The ST and RCM simulations were conducted assuming a closed homogeneous batch reactor. For the ST simulations, the definition of IDT is the same as that defined in the experiments discussed above. The exeprimental reflected shock pressure and temperature are used as the initial pressure and temperature in the simulations. To simulate the RCM experimental results, volume-time profiles obtained from non-reactive pressure trace are used to account for the non-ideal heat loss effects that occur during and after compression. All of the non-reactive volume-time histories are provided as Supplementary material.

Sensitivity and flux analyses are used to delineate the key reaction pathways leading to the formation of various major intermediate and final products for the pyrolysis and ignition of the fuel at different operating conditions. The IDT sensitivity analyses are performed using "brute force" sensitivity coefficient defined as:

$$S = \frac{In(\tau+/\tau-)}{In(k+/k-)} = \frac{In(\tau+/\tau-)}{In(2.0/0.5)}$$

where τ_+ and τ_- represents the IDTs obtained by increasing and reducing the reaction rate constant of each reaction by a factor of two. A negative sensitivity coefficient implies to a reaction promoting reactivity, whereas a positive sensitivity coefficient implies to a reaction inhibiting reactivity. Flux analyses are executed at the time corresponding to 10% of the fuel consumed.

4. Results and discussion

The experimental IDTs, pyrolysis speciation profiles and LFS comparisons for the two C_3H_4 isomers are shown in the sections below and are compared with the model predictions using NUIGMech1,2. The simulation results using AramcoMech3.0 [40] are also performed to show the model improvements using NUIGMech1.2. The important reactions for pyrolysis, ignition and high temperature oxidation process are identified and discussed through the brute-force sensitivity as well as flux analyses.

4.1. Pyrolysis comparisons of C_3H_4-a and C_3H_4-p

To obtain a fundamental knowledge of the initial breakdown of the C_3H_4 isomers, Fig. 3 presents comparisons between the computed and experimental species profiles formed in the pyrolysis of C_3H_4-a and C_3H_4-p obtained using two different SPSTs. In our previous work [25], the major and minor species from the pyrolysis of 2% C_3H_4-p were measured in the NUIG-SPST in the temperature range 1000–1800 K, at $p_C = 2$ bar. In the present study, these experiments have been extended to 5 bar pressure using the NUC-SPST. New C_3H_4-a pyrolysis experiments were also carried out at pressures of 2 and 5 bar using the NUIG-SPST and NUC-SPST, respectively in the temperature range 1000–1700 K. The pyrolysis data for C_3H_4-a and C_3H_4-p investigated in this work along with the C_3H_4-p pyrolysis measurements from our prior work [25] are all presented in Fig. 3.

The NUIGMech1.2 concentration profile predictions show good agreement with the important reactants and products species detected experimentally including C_3H_4-a, C_3H_4-p, CH_4, C_2H_2, C_6H_6, propene (C_3H_6), C_2H_4, 1,3-butadiene (C_4H_6), vinyl acetylene (C_4H_4) and di-acetylene (C_4H_2). On the contrary, large discrepancies are observed compared to the experimental data for the AramcoMech3.0 [40] predictions, Fig. 4a. NUIGMech1.2 and AramcoMech3.0 both under-predict ethylene formation in the pyrolysis experiments. Figure S2 of the Supplementary material compares the simulated major and minor species profiles calculated using AramcoMech3.0 [40] and NUIGMech1.2 with the experimental measurements for all of the operating conditions studied here.

The mutual isomerization reaction between allene and propyne plays an important role in the early consumption of the C_3H_4 isomers. Thus, model predictions are very sensitive to variations/uncertainties in their thermochemistry values. Table 4 compares the heats of formation of C_3H_4-a and C_3H_4-p at 298 K used in the NUIGMech mechanisms to those calculated by Miller and Klippenstein [43] and available in the Active Thermochemical Tables (ATcT) [56]. The thermochemistry of C_3H_4-a and C_3H_4-p used in NUIGMech1.2 are taken from the ATcT. The thermochemistry of C_3H_4-a has been updated to be consistent with the theoretical heat of formation (45.3 kcal mol^{-1}at 298 K) calculated by Miller and Klippenstein [43]. This decreases the heat of formation of allene by 0.3 kcal mol^{-1} relative to the original value and makes C_3H_4-a more stable, shifting the C_3H_4-a $\rightleftharpoons$ C_3H_4-p equilibrium towards C_3H_4-a leading to a decrease in the rate of consumption of C_3H_4-a. This results in the better predictions of the C_3H_4-a pyrolysis experiments presented in Fig. 4(b). Furthermore, C_3H_4-a dissociates faster than C_3H_4-p during pyrolysis, Fig. 4(b). The C–H bond dissociation energy (BDE) in C_3H_4-a is 88.7 ± 3 kcal mol^{-1} for $CH_{2=C=CH-H}$, while the C–H BDE in C_3H_4-p is 88.9 ± 1 kcal mol^{-1} for CH≡C–CH_2–H [57]. Due to the similar C–H BDEs of C_3H_4-a and C_3H_4-p, the isomerization reaction C_3H_4-a $\rightleftharpoons$ C_3H_4-p becomes more important in governing the pyrolysis of the C_3H_4 isomers. Figure 5 shows the dominant reactions responsible for the destructions of C_3H_4-a and C_3H_4-p during pyrolysis at 1450 K and at$p_C = 5$ bar. It is observed that the C_3H_4-a $\rightleftharpoons$ C_3H_4-p equilibrium dominates their consumption in the early stages. Since C_3H_4-p is thermodynamically more stable than C_3H_4-a, this reaction equilibrates very quickly during pyrolysis [43], leading to a faster rate of consumption of C_3H_4-a compared to C_3H_4-p. Subsequently, the individual dissociation reactions C_3H_4-p ↔ $\dot{C}_3H_3$ + $\dot{H}$ and C_3H_4-a ↔ $\dot{C}_3H_3$ + $\dot{H}$ become critical in the formation of the major products. A comparison of C_3H_4-a and C_3H_4-p pyrolysis data in Fig. 3 indicates the formation of equal quantities of intermediate and major product yields from both C_3H_4 isomers.

Figure 6 presents comparisons of concentration profiles of the two major products C_2H_2 and CH_4 from the pyrolysis of the C_3H_4 isomers performed at pressures of 2 and 5 bar and at residence times (τ) of 3.2 and 1.5 ms, respectively. Both the experimental data and simulation results show that equal quantities of C_2H_2 and CH_4 are formed from the pyrolysis of C_3H_4-a and C_3H_4-p, although discrepancies are observed in the C_2H_2 measurements for the 5 bar case, specifically at higher temperatures (> 1450 K) which can be explained by the relatively low carbon balance (slightly less than 90%) quantified in the standard GC method at the 5 bar condition. An analysis of the important reactions responsible for the destruction of both C_3H_4 isomers and the formation of C_2H_2 as a function of time are shown in Fig. 5. The formation of the major products C_2H_2 and CH_4 are controlled by the dissociation reactions C_3H_4-p ↔ $\dot{C}_3H_3$ + $\dot{H}$ and C_3H_4-a ↔ $\dot{C}_3H_3$ + $\dot{H}$ which produce $\dot{H}$ atoms. These react with both of the C_3H_4 isomers forming C_2H_2, via the chemically activated pathways C_3H_4-p + $\dot{H}$ ↔ C_2H_2 + $\dot{C}H_3$ and C_3H_4-a + $\dot{H}$ ↔ C_2H_2 + $\dot{C}H_3$, with the former reaction being the major contributor to C_2H_2 production. $\dot{C}H_3$ radicals subsequently abstract H-atoms from the C_3H_4 isomers to produce CH_4.

Figure 7 shows the integrated reaction pathway analysis at 1450 K and $p_C = 5$ bar for the pyrolysis of both C_3H_4-a and C_3H_4-p. The red color values correspond to fluxes through C_3H_4-a and the blue colors represent those through C_3H_4-p. It is observed that C_3H_4-p and C_3H_4-a contribute ~24.2% and ~30.2%, respectively to the total flux of C_2H_2 formation. Moreover, the production of CH_4 accounts for ~16.4% and ~15.9% of the total flux in the pyrolysis of C_3H_4-p and C_3H_4-a, respectively, via H-atom abstraction by $\dot{C}H_3$ radicals. We further performed sensitivity analyses to the production of C_2H_2 and CH_4 from the pyrolysis of C_3H_4-p and C_3H_4-a at 1450 K and $p_C = 5$ bar, Fig. S4. It is observed that C_3H_4-p ↔

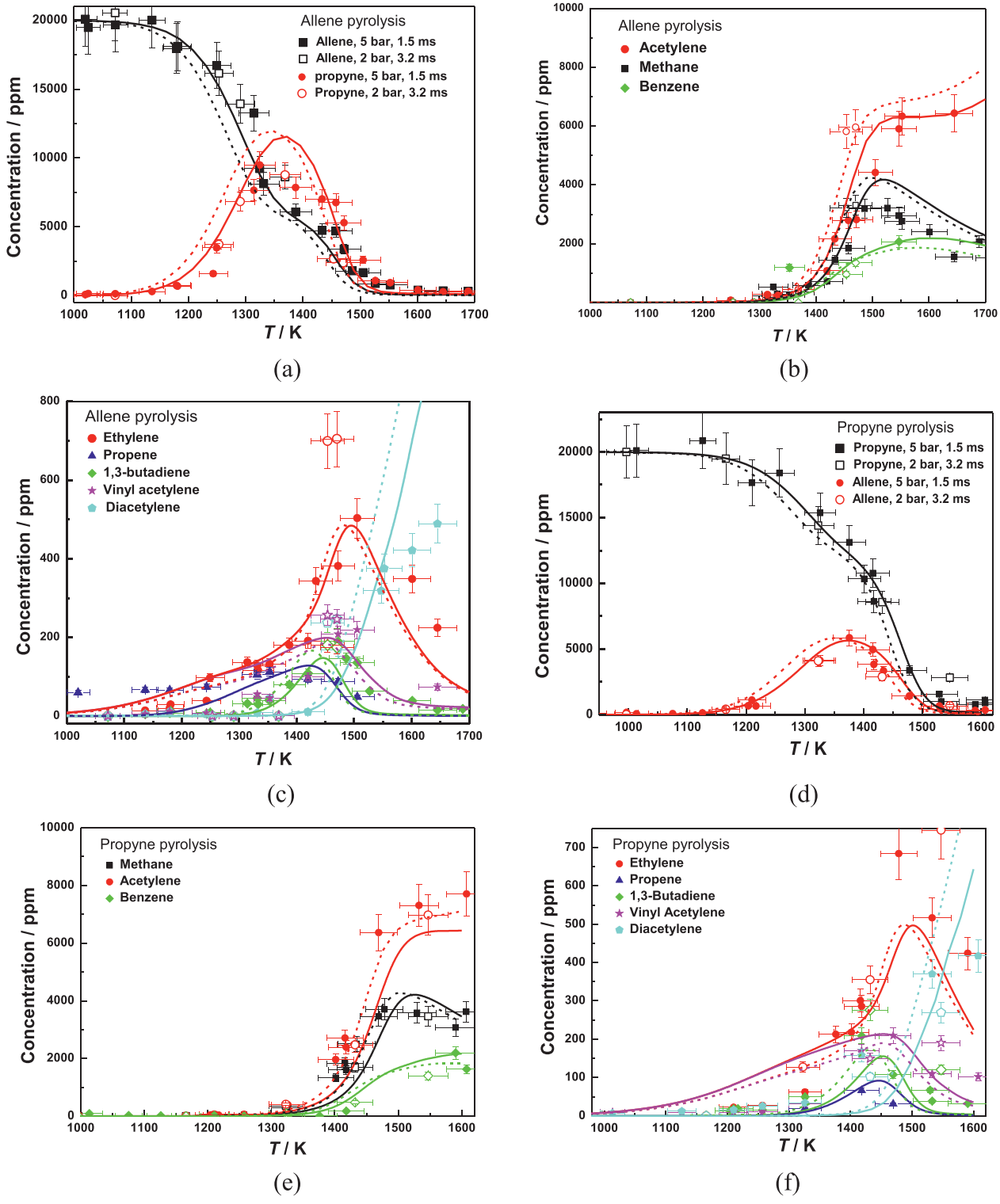

Fig. 3. Species concentration profiles for C_3H_4-a (a–c) and C_3H_4-p (d–f) pyrolysis at 2 bar and 5 bar pressures. Solid symbols and open symbols represent experimental data at 5 bar and 2 bar, respectively, solid lines and dashed lines correspond to the current model (NUIGMech1.2) predictions at 5 bar and 2 bar, respectively.

Table 4
Heat of formation values for C_3H_4-a and C_3H_4-p.

Species	$\Delta H_{f,0}$ (298 K) (kcal mol^{-1})			
	NUIGMech1.1	NUIGMech1.2	Miller and Klippenstein [43]	ATcT [56]
C_3H_4-a	45.6	45.3	45.3	45.3
C_3H_4-p	44.3	44.3	44.2	44.3

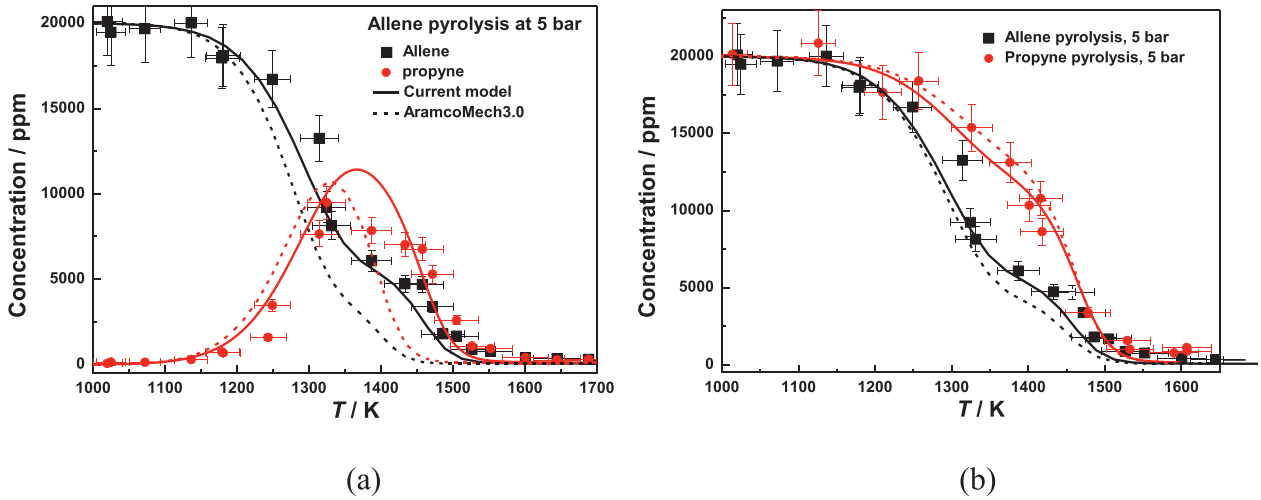

Fig. 4. (a) Comparison between model predictions by current mechanism and AramcoMech3.0 for the pyrolysis of C_3H_4-a at 5 bar, (b) Effect of thermochemistry of C_3H_4-a on the concentration profiles of C_3H_4-a and C_3H_4-p, dashed lines correspond to $\Delta H_{f,0}$ (298 K) = 45.6 kcal mol^{-1}, and solid lines correspond to $\Delta H_{f,0}$ (298 K) = 45.3 kcal mol^{-1}.

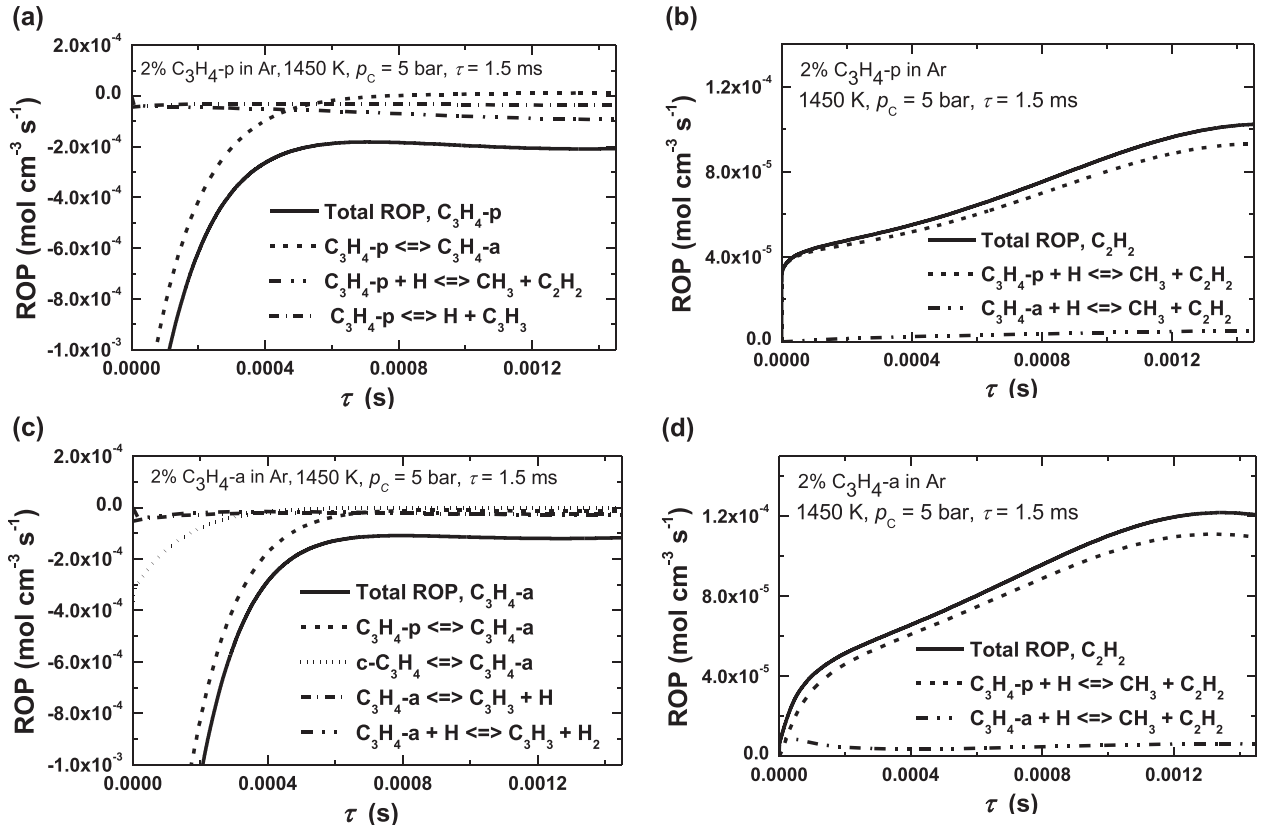

Fig. 5. ROP analyses of the important reactions responsible for the destruction and formation of the C_3H_4 isomers as well as C_2H_2 during the pyrolysis of (a), (b) C_3H_4-p and (c), (d) C_3H_4-a.

$\dot{C}_3H_3 + \dot{H}$ and C_3H_4-a $\leftrightarrow \dot{C}_3H_3 + \dot{H}$ are the most sensitive reactions highlighting the importance of the fuel dissociation reactions to the formation of the major product species. Furthermore, the same set of reactions are found to be sensitive to the formation of C_2H_2 and CH_4 in the pyrolysis of C_3H_4-p and C_3H_4-a. Figure S5 compares the rate constants of the most positive sensitive reactions $\dot{C}_3H_3 + \dot{H} \leftrightarrow C_3H_4$-p and $\dot{C}_3H_3 + \dot{H} \leftrightarrow C_3H_4$-a as well as the most negative sensitive reactions C_3H_4-p $+ \dot{H} \leftrightarrow \dot{C}_3H_3 + H_2$ and C_3H_4-a $+ \dot{H} \leftrightarrow \dot{C}_3H_3 + H_2$. The rate coefficient for $\dot{C}_3H_3 + \dot{H} \leftrightarrow C_3H_4$-a is only lower by a factor of less than 1.55 compared to that for $\dot{C}_3H_3 + \dot{H} \leftrightarrow C_3H_4$-p, while the rate coefficients for H-atom abstraction by $\dot{H}$ atoms from C_3H_4-p and C_3H_4-a are within ~40% of one another.

In NUIGMech1.2 the rate constant coefficients for $\dot{C}_3H_3 + \dot{H} \leftrightarrow C_3H_4$-p and $\dot{C}_3H_3 + \dot{H} \leftrightarrow C_3H_4$-a are taken from the calculations by Miller and Klippenstein [43], which are approximately a factor of 4.5 lower than the rate constants utilized in AramcoMech3.0 at 1500 K. Updating these rate constants in the current model leads to a significant improvement in the predictions of the pyrolysis profiles as shown in Figs. 4(a) and S2. C_3H_4-p and C_3H_4-

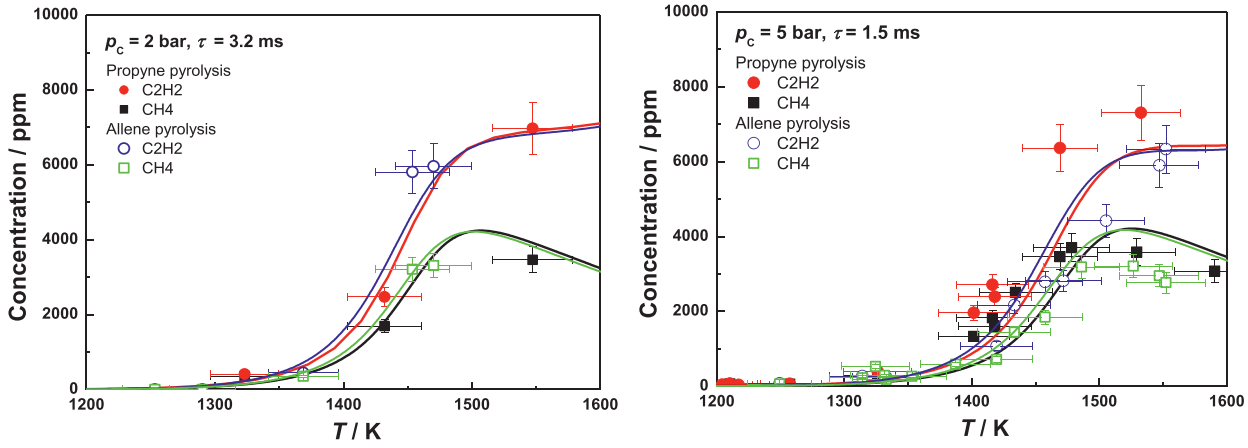

Fig. 6. Comparisons of the measured and the predicted concentration profiles of C_2H_2 and CH_4 from the pyrolysis of C_3H_4 isomers at (a) p_C = 2 bar, τ = 3.2 ms, and at (b) p_C = 5 bar, τ = 1.5 ms.

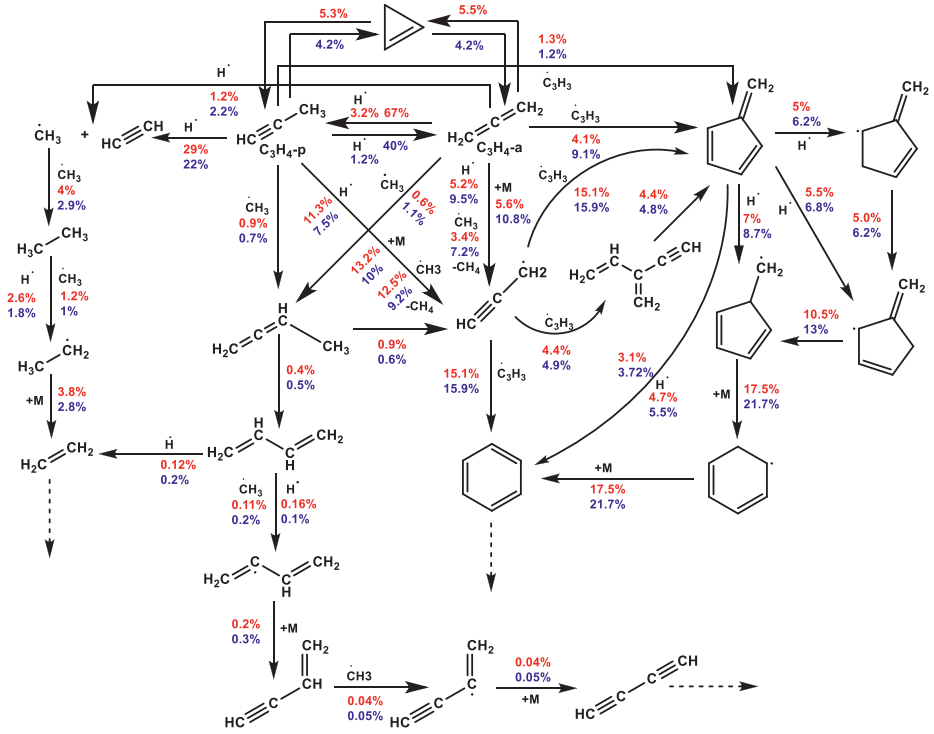

Fig. 7. Integrated reaction pathway analyses at 1450 K and p_C = 5 bar for the pyrolysis of C_3H_4-p (blue) and C_3H_4-a (red). (For interpretation of the references to color in this figure legend, the reader is referred to the web version of this article.)

a are also consumed by H-atom abstraction reactions by $\dot{H}$ and $\dot{C}H_3$ radicals, leading to the formation of $\dot{C}_3H_3$ radicals, and H_2 and CH_4, respectively. Most of the $\dot{C}_3H_3$ radicals recombine to produce benzene (C_6H_6) and fulvene. The formation of considerable quantities of C_6H_6 from the pyrolysis of C_3H_4-a and C_3H_4-p can be seen in Fig. 3. However, the yield of fulvene is low throughout the pyrolysis process. This is because fulvene subsequently contributes to the formation of C_6H_6, via the fulvene $\rightleftharpoons$ C_6H_6 and fulvene + $\dot{H}$ $\leftrightarrow$ C_6H_6 + $\dot{H}$ reactions. Fulvene also produces C_6H_6 via the formation of methylcyclopentadiene radicals ($\dot{C}_5H_5CH_2$–1, $\dot{C}_5H_5CH_2$–2, $\dot{C}_5H_5CH_2$) followed by $\dot{C}_5H_5CH_2$ = Cy$\dot{C}_6H_7$ and Cy$\dot{C}_6H_7$ $\leftrightarrow$ C_6H_6 + $\dot{H}$. In the pyrolysis process, C_2H_2 is generated from the chemically activated reactions of C_3H_4-a and C_3H_4-p with $\dot{H}$ atoms, C_3H_4-a + $\dot{H}$ $\leftrightarrow$ C_2H_2 + $\dot{C}H_3$ and C_3H_4-p + $\dot{H}$ $\leftrightarrow$ C_2H_2 + $\dot{C}H_3$. The methyl radicals produced recombine to form ethane, which in turn, undergoes H-atom abstraction by $\dot{H}$ atoms and $\dot{C}H_3$ radicals producing ethyl ($\dot{C}_2H_5$) radicals. These decompose to produce ethylene (C_2H_4) and $\dot{H}$ atoms. Small amounts of $\dot{C}H_3$ radicals add to C_3H_4-a and C_3H_4-p forming 1,2-C_4H_6, which then produces 1,3-C_4H_6, C_4H_4 and C_4H_2 through the reaction sequence 1,2-C_4H_6 $\rightarrow$ 1,3-C_4H_6 $\rightarrow$ $\dot{C}_4H_5$-i $\rightarrow$ C_4H_4 $\rightarrow$ $\dot{C}_4H_3$-i $\rightarrow$ C_4H_2 as illustrated in Fig. 5.

4.2. IDT behavior of C_3H_4-a and C_3H_4-p

IDTs of C_3H_4-p in ‘air’ were investigated in our previous work [25] using the NUIG RCM and HPST at equivalence ratios of 0.5, 1.0, and 2.0, at pressures of 10 and 30 bar, in the temperature range 690–1450 K. In that work NUIGMech1.1 was shown to predict these experimental data very well. In the present work, the IDT measurements of C_3H_4-a in ‘air’ are performed at the same conditions and the detailed kinetic mechanism is extended by incorporating the low-temperature chemistry for C_3H_4-a. In Fig. 8

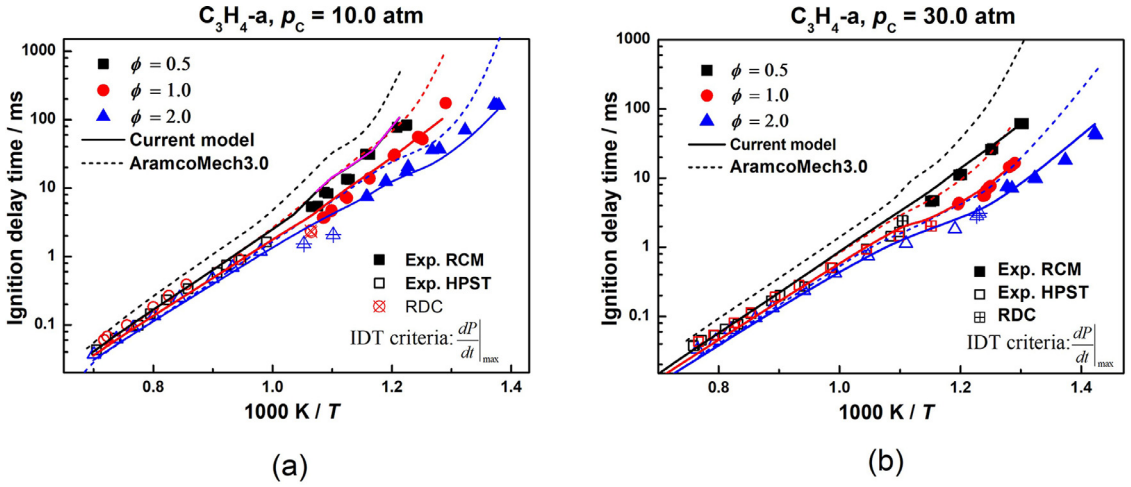

Fig. 8. IDT measurements of C_3H_4-a/'air' mixtures at 10 bar (a) and 30 bar (b); Simulations: solid lines are current model and short dash lines are AromacMech3.0 [40].

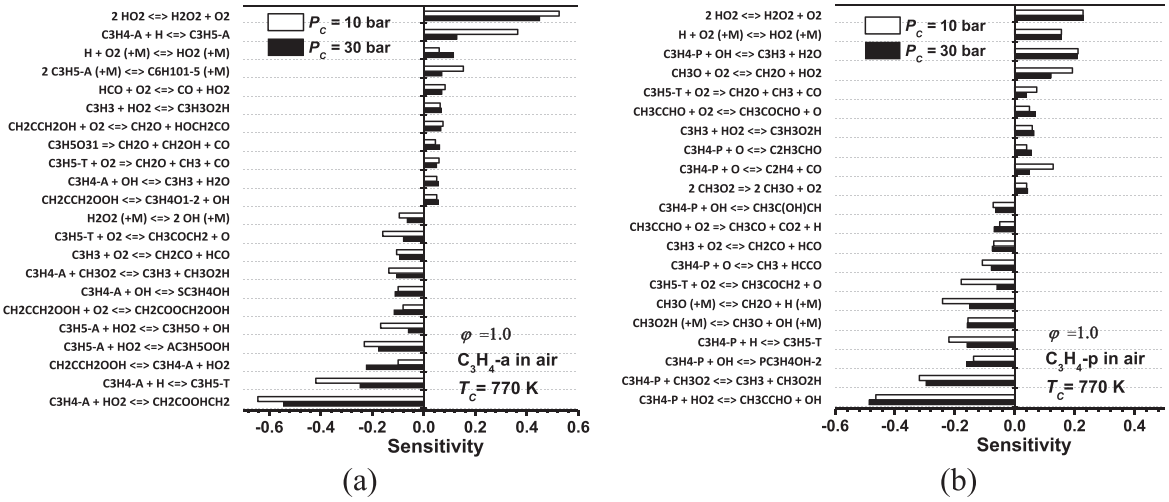

Fig. 9. Sensitivity analyses of IDTs for (a) C_3H_4-a and (b) C_3H_4-p at 770 K for 10 bar and 30 bar pressures.

the measured IDT data for C_3H_4-a are compared to the simulations using NUIGMech1.2 and AramcoMech3.0 [40]. The simulations using NUIGMech1.2 (solid lines) show much improved agreement compared to those using AramcoMech3.0 [40] (dashed lines).

To identify the dominant reactions in C_3H_4-a ignition, flux analyses were performed at $\varphi = 1.0$ in 'air' and 770 K for 10 bar and 30 bar pressures and at the time of 10% C_3H_4-a consumed, Fig. 10. The black color percentage values correspond to the flux at $p = 10$ bar, and the red color values corresponds to the flux at $p = 30$ bar with these values normalized to the amount of C_3H_4-a consumed. Sensitivity analyses were also carried out to point out the dominant reactions occurring during C_3H_4-a oxidation at 770 K for 10 bar and 30 bar pressures, Fig. 9(a).

Based on the current mechanism, at 770 K C_3H_4-a consumption commences via H-atom abstraction by $\dot{O}H$ and $H\dot{O}_2$ radicals forming $\dot{C}_3H_3$ radicals. Besides H-atom abstraction, $\dot{O}H$ radical addition to the double bond accounts for a large fraction of fuel consumption, it being almost 37% at 10 bar and 47% at 30 bar. The rate constant for this reaction is taken from the recent theoretical study of Zádor et al. [49], who performed a high-level ab-initio calculation using the UCCSD(T)-F12b/cc-pVQZ-F12//M06-2X/6-311++$G(d,p)$ level of theory. Flux analysis shows that $\dot{O}H$ addition to the terminal carbon atom forming $CH_2\dot{C}CH_2OH$ is the dominant fuel consumption pathway. Approximately 20% of the total flux goes through the addition of $CH_2\dot{C}CH_2OH$ radicals to O_2 to produce $CH_2C(O\dot{O})CH_2OH$ radicals at 10 bar, while $CH_2\dot{C}CH_2OH$ radical addition to O_2 producing CH_2O via the reaction: $CH_2\dot{C}CH_2OH + O_2 \leftrightarrow CH_2O + CH_2(OH)\dot{C}O$ accounts for the remaining 11% of the total flux. $CH_2C(O\dot{O})CH_2OH$ radical undergoes an internal H-atom transfer reaction to form $CH_2C(OOH)CH_2\dot{O}$ radicals and eventually generate ketene (CH_2CO), formaldehyde (CH_2O) and $\dot{O}H$ radicals via β-scission. In the present model the rate constants for$CH_2\dot{C}CH_2OH$ addition to O_2 is included by analogy with the 1-methyl-vinyl + O_2 reaction calculated by Chen et al. [42]. The rate constants for the subsequent internal H-atom transfer isomerization is adopted by analogy to the H-atom transfer isomerization reaction $CH_3CH(O\dot{O})CH_2OH \leftrightarrow CH_3CH(OOH)CH_2\dot{O}$ from Lizardo-Huerta et al. [58]. This is justified by the similar O–H BDE of 107 kcal mol^{-1} in $CH_2C(O\dot{O})CH_2OH$ compared to 105 kcal mol^{-1} in $CH_3CH(O\dot{O})CH_2OH$ [59]. The rate constant for $CH_2C(OOH)CH_2\dot{O} \rightarrow CH_2O + CH_2CO + \dot{O}H$ is adopted by analogy with $CH_3CH(OOH)CH_2\dot{O} \rightarrow CH_2O + CH_3CHO + \dot{O}H$ from Lizardo-Huerta et al. [58]. There is no study available for the rate constants of $CH_2C(OOH)CH_2\dot{O} \rightarrow CH_2O + CH_2CO + \dot{O}H$ and $CH_2C(O\dot{O})CH_2OH \leftrightarrow CH_2C(OOH)CH_2\dot{O}$. Furthermore, there are no significant changes in predicted IDTs even if the current rate constants of $CH_2C(O\dot{O})CH_2OH \leftrightarrow CH_2C(OOH)CH_2\dot{O}$ and $CH_2C(OOH)CH_2\dot{O} \rightarrow CH_2O + CH_2CO + \dot{O}H$ are reduced or increased by a factor of five, as shown in Fig. S6, indicating the insignificance of these reactions in the IDT predictions of C_3H_4-a/'air' mixtures.

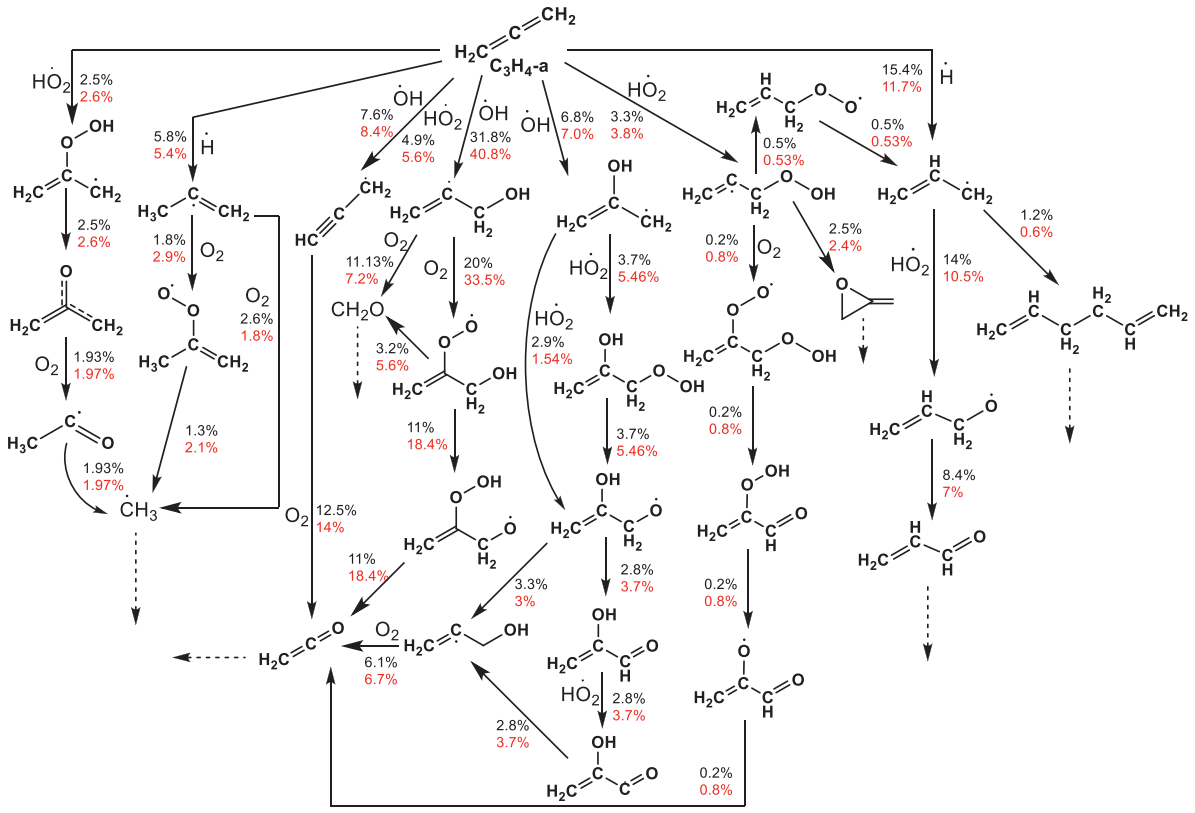

Fig. 10. Flux analyses for C_3H_4-a ignition at $\varphi = 1.0$ in 'air' at 770 K and at 10% C_3H_4-a consumed. The black color corresponds to the flux at 10 bar and the red color to that at 30 bar. (For interpretation of the references to color in this figure legend, the reader is referred to the web version of this article.)

Thus, implementing the actual rates would not affect the current model performance.

ȮH radical addition to the central carbon atom producing $CH_2COH\dot{C}H_2$ radicals accounts for ~7% of C_3H_4-a consumption. As $H\dot{O}_2$ radicals are more effective in reacting with allylic radicals, in the present mechanism the rate coefficients for the consumption of $CH_2COH\dot{C}H_2$ by hydroperoxyl radicals are assumed to be analogous to $\dot{C}_3H_5$-a + $H\dot{O}_2$ reactions calculated by Goldsmith et al. [60]. Figures 9(a) and 10 indicate that Ḣ atom addition to C_3H_4-a and subsequent reactions of the radicals formed have also a major role in controlling the fuel reactivity at low temperatures. The formation of $\dot{C}_3H_5$-t promotes overall reactivity, while the formation of $\dot{C}_3H_5$-a radicals inhibits reactivity, Fig. 9(a). Miller et al. [48] studied the C_3H_5 PES which includes the reactions C_3H_4-a + Ḣ ↔ $\dot{C}_3H_5$-a and C_3H_4-a + Ḣ ↔ $\dot{C}_3H_5$-t. NUIGMech1.2 includes the rate constants for the C_3H_4-a + Ḣ reactions as calculated by Miller et al. [48]. The $\dot{C}_3H_5$-t radicals so produced add to O_2 and subsequently decompose to CH_2O, CO and $\dot{C}H_3$ radicals, while allyl radicals can either react with hydroperoxyl radicals forming allyl-oxy and hydroxyl radicals or recombine to generate 1,5-hexadyne (C_6H_{10}–15), inhibiting reactivity.

From the sensitivity analyses presented in Fig. 9(a) it is observed that the inclusion of the C_3H_4-a + $H\dot{O}_2$ reactions are the most important in promoting the reactivity of C_3H_4-a. The rate constants for $H\dot{O}_2$ addition to the central carbon atom of C_3H_4-a are determined in this study by utilizing the energies of the $C_3H_5O_2$ potential energy surface (PES) calculated by Chen and Goldsmith [42] at the CCSD(*T*)-F12a/cc-pVTZ-F12 level of theory. We have calculated the partition functions of various intermediates, transition states and products using a 1-D hindered rotor treatment at the B2LYPD3/cc-pVTZ level of theory. The rate constants are determined using RRKM theory using the master equation system solver program, MESS [61]. The potential energy surfaces and the corresponding rate constants are presented in Figs. 11 and 12. According to Figs. 11 and 12, C_3H_4-a + $H\dot{O}_2$ ↔ $CH_2C(OOH)\dot{C}H_2$ and C_3H_4-a + $H\dot{O}_2$ ↔ $CH_2C(O\dot{O})CH_3$ are the competitive reaction channels. The intermediate $CH_2C(OOH)\dot{C}H_2$ produces $CH_2C(O\dot{O})CH_3$ through isomerization and the product $\dot{C}H_2COOH + \dot{O}H$ by O–O bond dissociation. Due to the very high reaction barrier of the $CH_2C(OOH)\dot{C}H_2$ ↔ $CH_2C(O\dot{O})CH_3$ channel, the major population of the intermediate $CH_2C(OOH)\dot{C}H_2$ produces the product $\dot{C}H_2COOH + \dot{O}H$ and is the dominant channel for $H\dot{O}_2$ addition to the central carbon atom in C_3H_4-a. Therefore, the isomerization channel $CH_2C(OOH)\dot{C}H_2$ ↔ $CH_2C(O\dot{O})CH_3$ is not the major reaction path in the C_3H_4-a + $H\dot{O}_2$ system. Moreover, the $CH_2C(O\dot{O})CH_3$ intermediate can produce four different products including $CH_3COOH + \dot{O}H$ in addition to $CH_2O + CH_3\dot{C}O$. Among these four different channels, $CH_2C(O\dot{O})CH_3$ ↔ $CH_2O + CH_3\dot{C}O$ is the major product. Figure 12 shows that at the low temperatures (< 700 K), the formation of $CH_2O + CH_3\dot{C}O$ via $CH_2C(O\dot{O})CH_3$ dominates, whereas at higher temperatures (> 700 K) $\dot{C}H_2COOH + \dot{O}H$ is the major product set produced through the $CH_2C(OOH)\dot{C}H_2$ intermediate. The $\dot{C}H_2COOH$ radical reacts with O_2 leading to the formation of CO_2, via $\dot{C}H_2COOH + O_2 \rightarrow CO_2 + CH_3\dot{C}O + \dot{H}$, and the rate constant for this reaction is estimated by analogy with the addition reaction of methylene ($\dot{C}H_2$) to O_2, $\dot{C}H_2 + O_2 \rightarrow CO_2 + \dot{H} + \dot{H}$. There is no study available for the interaction of $\dot{C}H_2COOH$ with O_2 and thus a further study of this system is required.

Another vital reaction channel promoting C_3H_4-a reactivity at lower temperature is the formation of the $CH_2\dot{C}H_2OOH$ adduct through the addition of $H\dot{O}_2$ radicals to the terminal carbon atom of C_3H_4-a. The rate constant for the terminal addition of $H\dot{O}_2$ to C_3H_4-a is adopted by analogy to the $\dot{Q}OOH$ ↔ alkene + $H\dot{O}_2$ reaction, specifically CC=ĊC(OOH)CCC ↔ CC=C=CCCC + $H\dot{O}_2$ from You et al. [62]. The $CH_2\dot{C}H_2OOH$ can add to O_2 followed by two

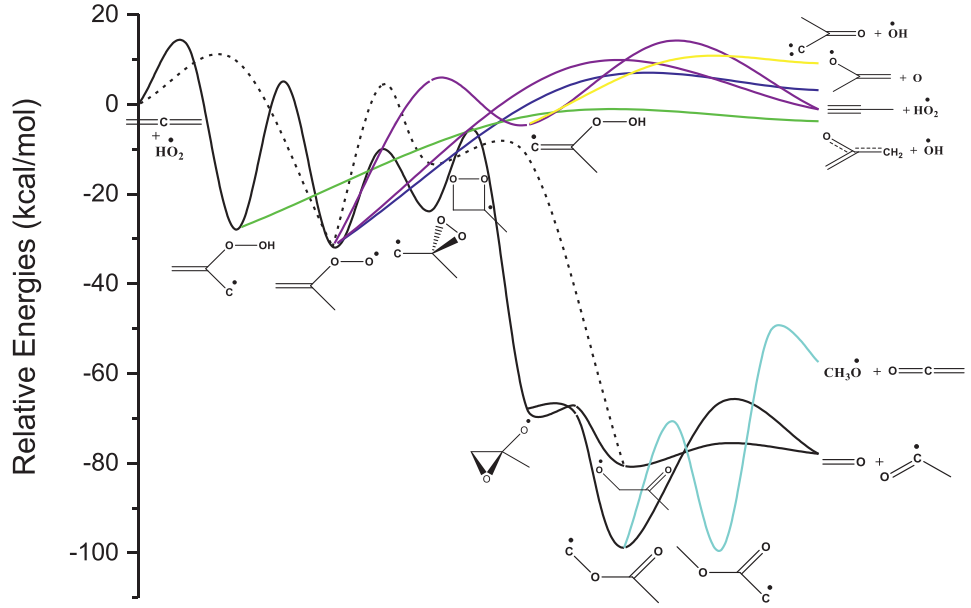

Fig. 11. The $C_3H_5O_2$ potential energy surface, relative to C_3H_4-*a* + $H\dot{O}_2$.

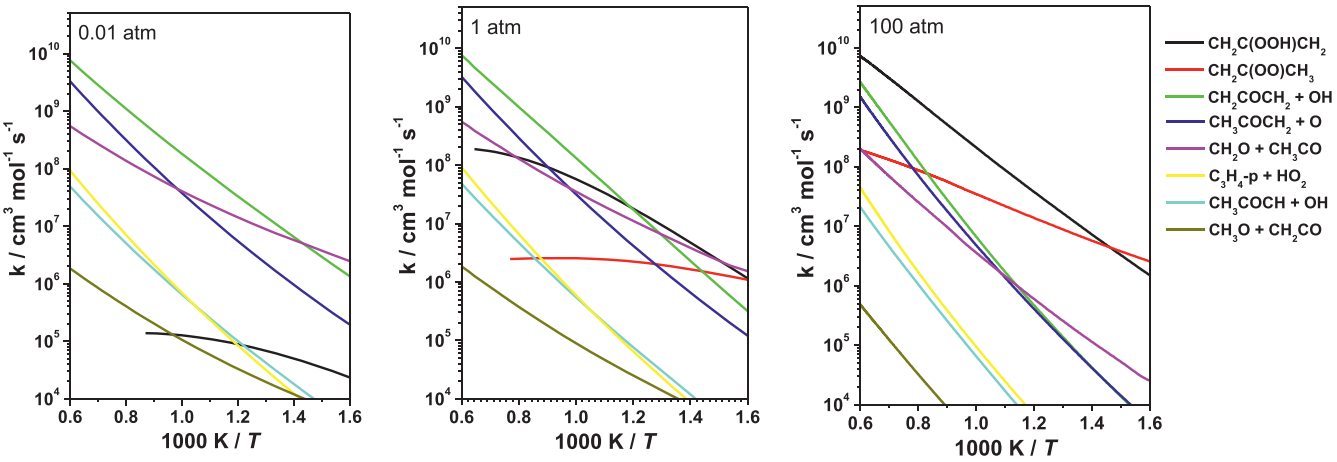

Fig. 12. Arrhenius plot for the various product channels formed during C_3H_4-*a* + $H\dot{O}_2$ at 0.01 atm, 1 atm and100 atm.

successive $\dot{O}H$ elimination reactions. In the current mechanism the rate constants for $CH_2\dot{C}CH_2OOH + O_2$ and the following reactions are estimated by analogy with the $CH_2{=}\dot{C}HCH_3 + O_2$ reactions calculated by Chen and Goldsmith [42] and by Goldsmith et al. [60] who investigated the $C_3H_7O_4$ PESs, respectively.

In our previous mechanisms [25,40] the above addition reactions of $\dot{O}H$ and $H\dot{O}_2$ radicals to C_3H_4-a together with their succeeding pathways were not considered. In the current mechanism we have included the C_3H_4-a + $H\dot{O}_2$ and C_3H_4-a + $\dot{O}H$ reaction systems as discussed above. These results reveal that although a lesser flux passes through the C_3H_4-a + $H\dot{O}_2$ pathways, the chain branching channel C_3H_4-a + $H\dot{O}_2 \leftrightarrow CH_2C(OOH)\dot{C}H_2 \leftrightarrow \dot{C}H_2CO\dot{C}H_2 + \dot{O}H$ is the most important reaction promoting the reactivity of C_3H_4-a. The effect on the IDT predictions for $\varphi = 2.0$ at 30 bar of incorporating the C_3H_4-a + $H\dot{O}_2$ reactions in NUIG-Mech1.2 is presented in Fig. 13. This illustrates the importance of the $H\dot{O}_2$ addition reactions. It should be noted that in the current mechanism the energy barrier of C_3H_4-a + $H\dot{O}_2 \leftrightarrow CH_2C(OOH)\dot{C}H_2$ has been decreased by 1.7 kcal/mol which increases the rate constant of this reaction by approximately a factor of two in the tem-

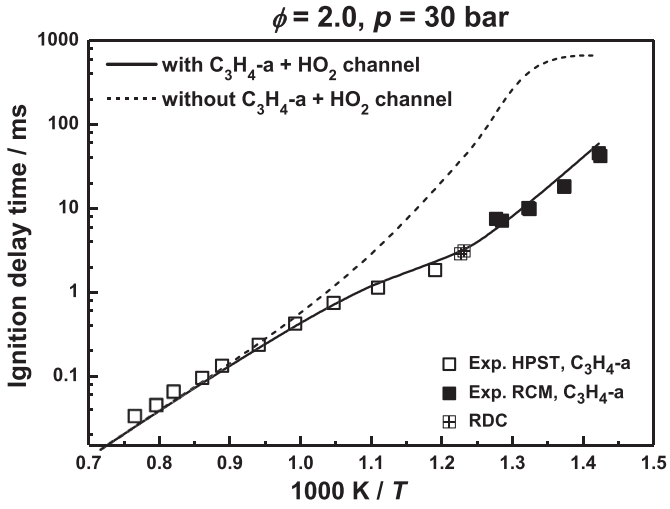

Fig. 13. Effect of C_3H_4-*a* + $H\dot{O}_2$ reaction on IDT prediction.

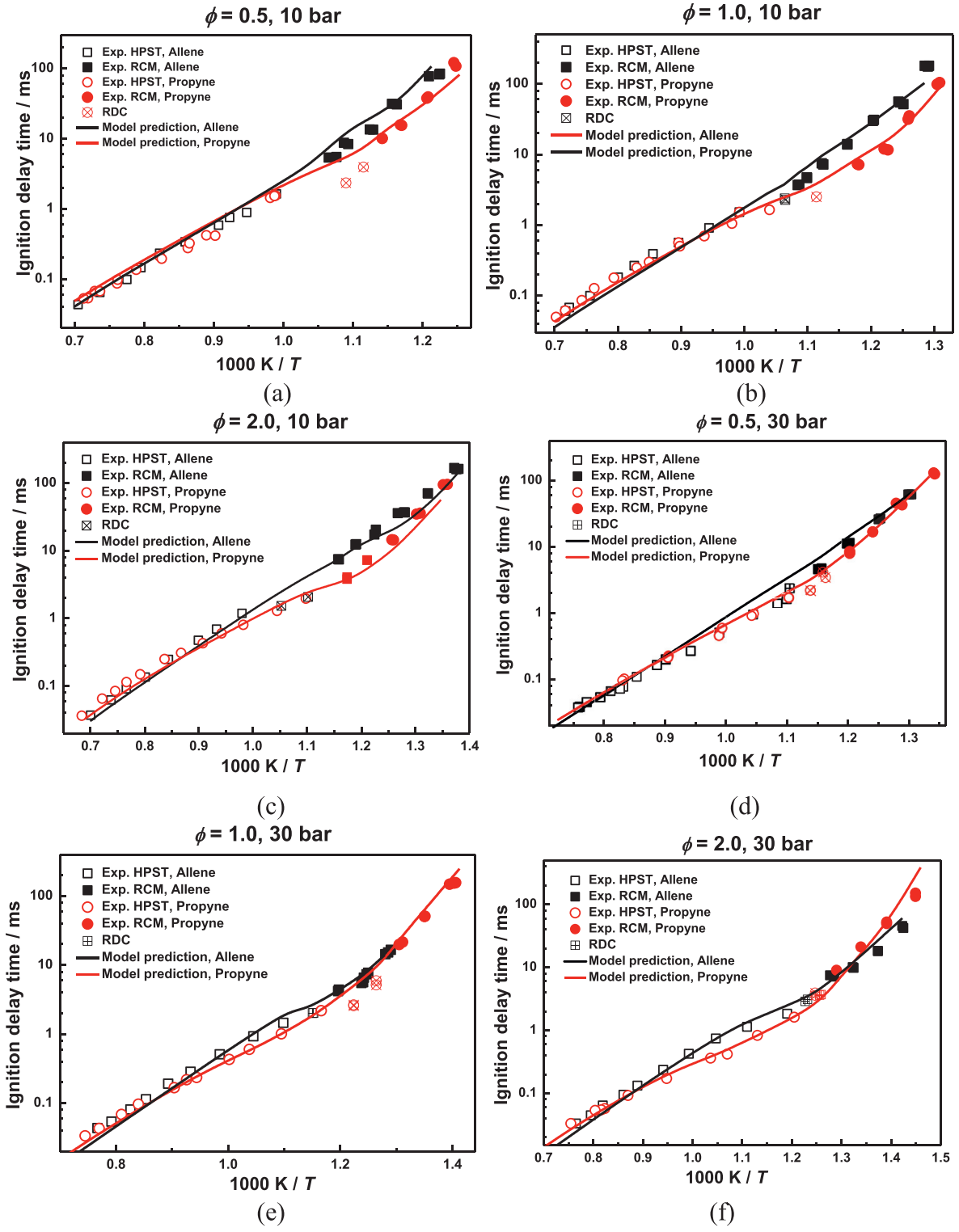

Fig. 14. Comparisons of IDT measurements of C_3H_4-a with previously published C_3H_4-p data [25] at equivalence ratios of 0.5, 1.0, and 2.0 in 'air' at pressures of 10 and 30 bar. Solid lines represent current model predictions.

perature range of 700 – 2000 K. This results in a better agreement of the model predictions with the experimental RCM IDT data.

To explore the kinetic features of the ignition of the C_3H_4 isomers, the IDT measurements of C_3H_4-a from the current study are compared with our previously published C_3H_4-p data [25] in Fig. 14 at equivalence ratios of 0.5, 1.0, and 2.0 in 'air' at pressures of 10 and 30 bar, in a wide range of temperature from 690 – 1450 K. The present updated kinetic mechanism accurately predicts the measured ST and RCM IDTs of the two fuels, for all operating conditions. Furthermore, both experimental and modeling results show that the two C_3H_4 isomers exhibit similar reactivities at high temperatures (1000–1450 K), whereas at intermediate temperatures (770–1000 K) C_3H_4-p is the fastest to ignite and this phenomenon is more pronounced at 10 bar compared to 30 bar. How-

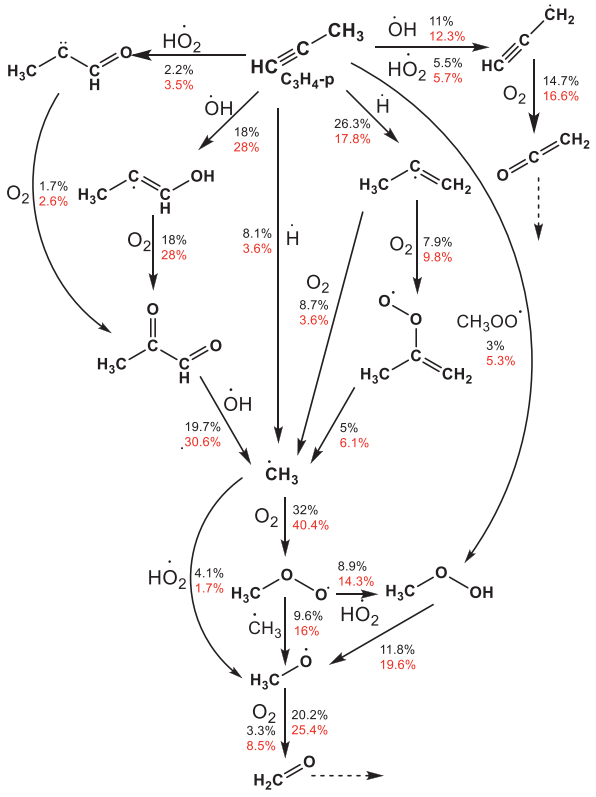

Fig. 15. Flux analyses for C_3H_4-p ignition at φ = 1.0 in 'air' at 770 K and at 10% C_3H_4-p consumed. The black color corresponds to the flux at 10 bar and red color to that at 30 bar. (For interpretation of the references to color in this figure legend, the reader is referred to the web version of this article.)

ever, this trend reverses at lower temperatures in the range 690–770 K, where C_3H_4-a is more reactive than C_3H_4-p, Fig. 14. In our previous study [25], the updated C_3H_4-p kinetic sub-mechanism published as NUIGMech1.1 was found to be in good agreement against the experimental IDT data measured in both the ST and RCM, and thus has been retained in our current model. For the sake of comparison, in Fig. 15, the important reaction channels for C_3H_4-p oxidation are illustrated through a flux analysis at φ = 1.0 in 'air' at 770 K at p_C = 10 bar and 30 bar.

Figures 9(b) and 15 show that the addition of $\dot{O}H$ and $H\dot{O}_2$ radicals to C_3H_4-p plays a major role in the accurate prediction of C_3H_4-p IDTs [25], similar to that discussed above for C_3H_4-a. Methyl radical is the most influential species in C_3H_4-p oxidation formed primarily from 2-oxo propanal decomposition and the chemically activated reaction C_3H_4-p + $\dot{H}$ ↔ C_2H_2 + $\dot{C}H_3$. The $\dot{C}_3H_5$-t radical produced by C_3H_4-p + $\dot{H}$ ↔ $\dot{C}_3H_5$-t also contributes significantly towards $\dot{C}H_3$ formation, via its addition to O_2. The resultant methyl radicals subsequently form $CH_3\dot{O}_2$ and CH_3O_2H as shown in Fig. 15. $CH_3\dot{O}_2$ radicals abstract hydrogen atoms from C_3H_4-p, while CH_3O_2H dissociates into $CH_3\dot{O}$ and $\dot{O}H$ radicals, ultimately enhancing the reactivity of the C_3H_4-p system. Thus, the formation of $\dot{C}_3H_5$-t, via $\dot{H}$ atom addition to both C_3H_4-a and C_3H_4-p promotes reactivity. As discussed earlier, in the case of C_3H_4-a it is competitive with C_3H_4-a + $\dot{H}$ ↔ $\dot{C}_3H_5$-a, which inhibits reactivity, Fig. 9(a). For C_3H_4-p the rate constant of C_3H_4-p + $\dot{H}$ ↔ $\dot{C}_3H_5$-a is not competitive with the other channels [48], and this leads to the faster ignition of C_3H_4-p compared to C_3H_4-a at intermediate temperatures (770–1000 K).

Figure 14 reveals that at intermediate temperatures, the difference between the IDTs for C_3H_4-a and C_3H_4-p is greater at 10 bar compared to that at 30 bar. Figures 9(a) and 10 show that in the case of C_3H_4-a, as the pressure increases to 30 bar, the percentage contribution of C_3H_4-a + $\dot{H}$ ↔ $\dot{C}_3H_5$-a and $\dot{C}_3H_5$-a + $\dot{C}_3H_5$-a ↔ C_6H_{10}-15 reduces, accounting for only 11.7% and 0.6% of the total flux, while at 10 bar their corresponding contributions are 15.4% and 1.2%, respectively. Simultaneously, the importance of the reaction C_3H_4-a + $H\dot{O}_2$ ↔ $CH_2\dot{C}CH_2OOH$ and subsequent reactions of the $CH_2\dot{C}CH_2OOH$ radical increases, promoting reactivity at 30 bar and leads to a decline in the difference in the reactivities of the two C_3H_4 isomers. The formation of $CH_2\dot{C}CH_2OOH$ and the resulting chain branching reactions producing two $\dot{O}H$ radicals are also responsible for the higher reactivity of C_3H_4-a at lower temperatures (690–770 K) at 30 bar and at φ = 2.0, Fig. 14(f). In contrast, at higher temperatures, the governing reactions for the oxidation of both C_3H_4-a and C_3H_4-p are similar. At high temperatures (1000–1450 K), the production of $\dot{C}_3H_3$ radicals by *H*-atom abstraction reactions becomes the dominant fuel consumption channel, and $\dot{C}_3H_3$ + O_2 ↔ CH_2CO + $H\dot{C}O$ is the most sensitive reaction promoting reactivity for both C_3H_4-a and C_3H_4-p.

4.3. LFSs comparisons for C_3H_4-a and C_3H_4-p

Figure 16(a) presents experimentally measured (using the UCF combustion vessel) and model predicted (using the present mechanism and AramcoMech3.0) LFSs for C_3H_4-a/'air' mixtures at an unburned temperature of T_U = 373 K and at pressures of 1 and 2 bar. Furthermore, in order to evaluate the effect of molecular structure of C_3H_4 isomers on the flame characteristics, the LFSs of C_3H_4-a and C_3H_4-p [25] are compared for T_U = 373 K at p_C = 1 and 2 bar over the entire range of equivalence ratios φ = 0.6 – 1.6 in Fig. 16(b). Figure 16(a) shows that the new updated mechanism better reproduces the C_3H_4-a data compared to AramcoMech3.0, which under-predicts the flame speed data significantly. However, slight discrepancies between the model predictions and experimental measurements for the C_3H_4-p flames are observed in Fig. 16(b). It can be seen that the maximum flame speed for C_3H_4-p flame is ~5 cm s^{-1} higher than that of C_3H_4-a at both 1 and 2 bar.

The most significant improvement in the model performance is achieved by adopting the rate coefficients calculated by Miller and Klippenstein [43] for both fuel dissociation reactions C_3H_4-p ↔ $\dot{C}_3H_3$ + $\dot{H}$ and C_3H_4-a ↔ $\dot{C}_3H_3$ + $\dot{H}$, and updating the rate constants in AramcoMech3.0 leads to a ~12% increase in the peak flame speed prediction as presented by the dash-dotted line in the Fig. 17. However, this is not the only change that has improved the flame speed performance. In NUIGMech1.2 the rate constant for $\dot{C}_3H_3$ + $\dot{O}H$ ↔ $\dot{C}_2H_3$ + $H\dot{C}O$ is adopted from the theoretical work by Vanuzzo et al. [54] which is a factor of ~1.3 higher than the rate constant estimated in AramcoMech3.0 in the high temperature range of 1000–2000 K, and thus, using the updated rate in AramcoMech3.0 further increase the peak flame speed by ~5% as depicted by the dot-dot-dashed line in the Fig. 17. The last agreement shown by the solid line is obtained by updating the Ö atom addition reactions to C_3H_4-a and C_3H_4-p in AramcoMech3.0 which further increased the peak flame speed prediction by ~7%. The C_3H_4-a + Ö and C_3H_4-p + Ö reaction channels are included in the mechanism from the theoretical study of Nguyen et al. [50] and Gimondi et al. [51], respectively. Nguyen et al. [50] determined that the addition of an Ö atom to the central and terminal carbon atoms in C_3H_4-a dominate at combustion relevant conditions. Ö atom addition to the central carbon in C_3H_4-a primarily generates $\dot{C}H_2$ (methylene) and CH_2CO (ketene), while addition to the terminal carbon produces allenyloxy radical ($\dot{C}_3H_3O$) + $\dot{H}$, reactions which were not included in AramcoMech3.0. Gimondi et al. [51] found that methylketenyl ($CH_3\dot{C}CO$) + $\dot{H}$ and $\dot{C}H_3$ + $H\dot{C}CO$ are the dominant channels produced from Ö atom addition to the terminal and central carbon atoms in C_3H_4-p. The C_3H_4-p + Ö ↔ $CH_3\dot{C}CO$ + $\dot{H}$

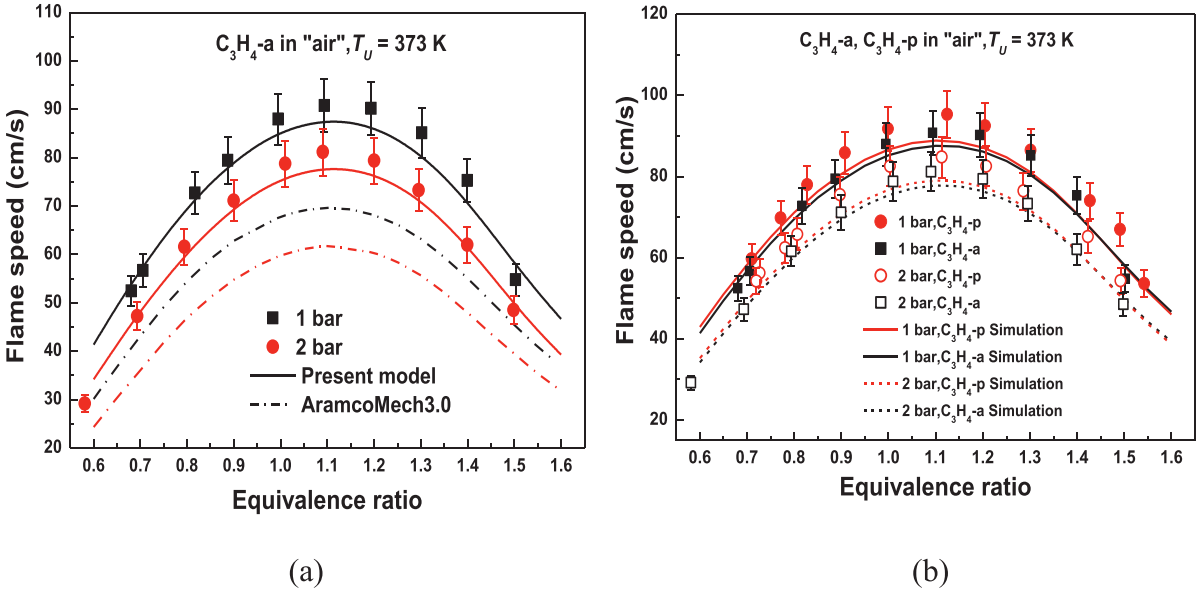

Fig. 16. (a) Comparisons of predicted LFSs by the present mechanism and AramcoMech3.0 against the flame speed measurements for C_3H_4-a/'air' mixtures (b) comparisons of C_3H_4-a/'air' and C_3H_4-p/'air' at an unburned temperature of T_U = 373 K and at pressure of 1 bar and 2 bar conditions.

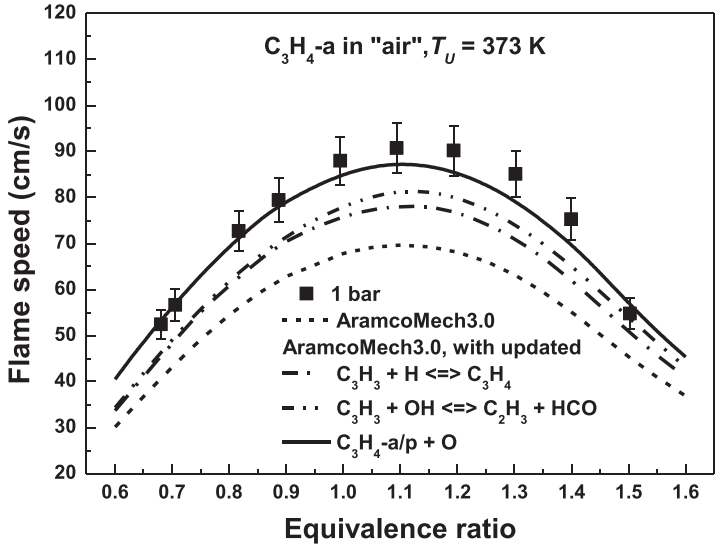

Fig. 17. Important reactions responsible for the improvement in the flame speed predictions using NUIGMech1.2 compared to AramcoMech3.0.

reaction channel was also not included in AramcoMech3.0. The aforementioned sets of reactions are also largely responsible for the improvement in the C_3H_4-p flame speed predictions, that is, the updates made in the rate constants of C_3H_4 dissociation reactions, $\dot{C}_3H_3 + \dot{O}H$ and C_3H_4-a + Ö reactions as well as the C_3H_4-p + Ö addition reactions in NUIGMech1.2 leads to the better agreement with C_3H_4-p flame speed experimental measurements.

To identify the key reactions influencing LFSs, flux and sensitivity analyses are performed in Fig. 18 for both C_3H_4-a and C_3H_4-p flames at φ = 1.1 and 1 bar pressure. The flux analyses indicate that the contribution of the major reaction pathways are essentially the same for both the C_3H_4-a and C_3H_4-p flames. According to the current mechanism, Ḣ atom assisted isomerization reaction between C_3H_4-a and C_3H_4-p, C_3H_4-p + Ḣ ↔ C_3H_4-a + Ḣ become important at the flame conditions. Moreover, other dominant reactions driving fuel consumption in both flames are the chemical activated channel C_3H_4-p + Ḣ ↔ $C_2H_2 + \dot{C}H_3$ as well as H-atom abstraction reactions by ȮH radicals and Ḣ atoms forming $\dot{C}_3H_3$ radicals. Although Ḣ atom addition reactions to C_3H_4-a and C_3H_4-p contribute little to fuel consumption, they become important at high-temperature flame conditions because they compete with the chain branching reaction $H\dot{} + O_2 \leftrightarrow$ Ö + ȮḢ in consuming Ḣ atoms. As shown in Fig. 18(b), at the stoichiometric condition, the C_3H_4-a + Ḣ ↔ $\dot{C}_3H_5$-a reaction strongly inhibits the flame speed of C_3H_4-a which accounts for 7% of the total flux, while for the C_3H_4-p flame, the contribution of this channel decreases to only 1%, Fig. 18(a). The resultant $\dot{C}_3H_5$-a consume Ḣ atoms via $\dot{C}_3H_5$-a + Ḣ ↔ C_3H_6 accounting for 4.3% of the total flux in the C_3H_4-a flame, while for the C_3H_4-p flame this reaction contributes only 0.5% to Ḣ atom consumption. The peak flame speed of allene is lower than propyne because it consumes high quantities of Ḣ atoms via: C_3H_4-a + Ḣ ↔ $\dot{C}_3H_5$-a and $\dot{C}_3H_5$-a + Ḣ ↔ C_3H_6 as shown in Fig. 18(a). Removing the $\dot{C}_3H_5$-a + Ḣ ↔ C_3H_6 reaction from the mechanism leads to the same flame speed predictions for both isomers as shown in the Fig. S7.

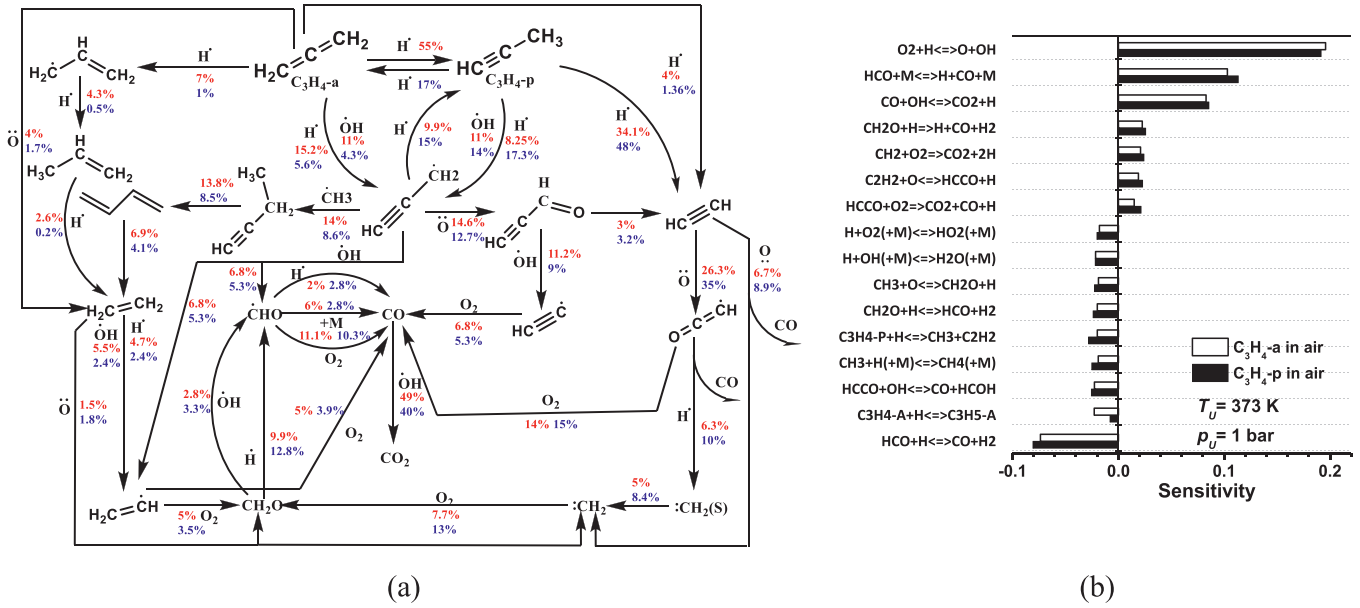

Fig. 18. (a) Flux analyses for flame speed of C_3H_4-a/'air' and C_3H_4-p/'air' mixtures, at 50% of fuel consumed. The red color corresponds to the flux for the C_3H_4-a flame and the blue color to the flux for the C_3H_4-p flame; (b) Sensitivity analyses to flame speed predictions for C_3H_4-a/'air' and C_3H_4-p/'air' mixtures at $\varphi = 1.0$, $p = 1$ bar and $T_U = 373$ K. (For interpretation of the references to color in this figure legend, the reader is referred to the web version of this article.)

5. Conclusions

In this study, new IDTs of C_3H_4-a/'air' mixtures were measured over a wide range of experimental conditions for the temperature range 690 – 1450 K at 10 bar and 30 bar pressure, and at equivalence ratios of $0.5 \leq \varphi \leq 2.0$. C_3H_4-a and C_3H_4-p pyrolysis were studied using a SPST in the temperature range of 1000–1700 K, at pressure of 2 and 5 bar. Additionally, LFSs of C_3H_4-a/'air' mixtures were also measured at elevated temperature conditions at equivalence ratios in the range 0.6–1.5. An updated kinetic mechanism, NUIGMech1.2, developed based on NUIGMech1.1, can predict all of the experimental results for both C_3H_4-a and C_3H_4-p. It is observed that C_3H_4-a dissociates faster than C_3H_4-p during pyrolysis. The mutual isomerization reaction $C_3H_4\text{-a} \rightleftharpoons C_3H_4\text{-p}$ governs the early stage of pyrolysis, and subsequently, the individual dissociation reactions $C_3H_4\text{-p} \leftrightarrow \dot{C}_3H_3 + \dot{H}$ and $C_3H_4\text{-a} \leftrightarrow \dot{C}_3H_3 + \dot{H}$ became important to the formation of the major products.

The two C_3H_4 isomers display similar IDTs at high temperatures (> 1000 K), while at intermediate temperatures (770 – 1000 K) C_3H_4-p is faster to ignite. At lower temperatures (< 770 K) C_3H_4-a is more reactive. For both isomers the addition reactions of $\dot{O}H$ and $H\dot{O}_2$ radicals to the fuel has the highest influence in promoting reactivity. This work reveals that although a lesser flux passes through the C_3H_4-a + $H\dot{O}_2$ the chain branching channel $C_3H_4\text{-a} + H\dot{O}_2 \leftrightarrow CH_2C(OOH)\dot{C}H_2 \leftrightarrow \dot{C}H_2CO\dot{C}H_2 + \dot{O}H$ is the most important reaction promoting the reactivity of C_3H_4-a. The interaction of $\dot{C}H_2CO\dot{C}H_2$ with O_2 is found to be important for the predictions of C_3H_4-a IDTs, however there is no study available for the $\dot{C}H_2CO\dot{C}H_2 + O_2$ reaction and thus a further study of this system is required. For C_3H_4-a, the rate of the reaction $C_3H_4\text{-a} + \dot{H} \leftrightarrow \dot{C}_3H_5\text{-a}$ is found to be competitive with that for $C_3H_4\text{-a} + \dot{H} \leftrightarrow \dot{C}_3H_5\text{-t}$, reducing the reactivity of C_3H_4-a at intermediate temperatures. At lower temperatures (< 770 K) the importance of the terminal addition of $H\dot{O}_2$ radicals to C_3H_4-a and subsequent reactions increases, promoting its reactivity. At higher temperatures (> 1000 K) the reaction $\dot{C}_3H_3 + O_2 \leftrightarrow CH_2CO + H\dot{C}O$ is found to be the most sensitive reaction controlling the reactivity for both C_3H_4-a and C_3H_4-p, and thus they have similar reactivities in this temperature regime. The maximum measured and predicted LFSs of C_3H_4-p are slightly higher than those for C_3H_4-a as $\dot{H}$ atom addition producing allyl radicals is more important in C_3H_4-a compared to C_3H_4-p and thus results in lower flame speeds for C_3H_4-a compared to C_3H_4-p.

Disclaimer

This report was prepared as an account of work sponsored by an agency of the United States Government. Neither the United States Government nor any agency thereof, nor any of their employees, makes any warranty, express or implied, or assumes any legal liability or responsibility for the accuracy, completeness, or usefulness of any information, apparatus, product, or process disclosed, or represents that its use would not infringe privately owned rights. Reference herein to any specific commercial product, process, or service by trade name, trademark, manufacturer, or otherwise does not necessarily constitute or imply its endorsement, recommendation, or favoring by the United States Government or any agency thereof. The views and opinions of authors expressed herein do not necessarily state or reflect those of the United States Government or any agency thereof.

Declaration of Competing Interest

The authors declare that they have no known competing financial interests or personal relationships that could have appeared to influence the work reported in this paper.

Acknowledgments

The authors acknowledge Science Foundation Ireland for funding via their Principal Investigator Program through project number 15/IA/3177 and 16/SP/3829. Jinhu Liang acknowledges the support from the National Natural Science Foundation of China (11602231), International Scientific Cooperation Projects of Key R&D Programs (201803D421101), Research Project supported by Shanxi Scholarship Council of China (2020115), and the Young Academic Leaders Support Program of North University of China (QX201810). The material for measuring flame speed is based upon

work supported by the U.S. Department of Energy's Office of Energy Efficiency and Renewable Energy (EERE) under Award Number DE-EE0007984 (Co-Optima).

Supplementary materials

Supplementary material associated with this article can be found, in the online version, at doi:10.1016/j.combustflame.2021.111578.

References

[1] P. Dagaut, M. Cathonnet, J.C. Boettner, F. Gaillard, Kinetic modeling of propane oxidation, Combust. Sci. Tech. 56 (1987) 23–63.
[2] P. Dagaut, M. Cathonnet, J.C. Boettner, Experimental study and kinetic modeling of propane oxidation in a jet stirred flow reactor, J. Phys. Chem. 92 (1988) 661–671.
[3] A. Chakir, M. Cathonnet, J.C. Boettner, F. Gaillard, Kinetic study of n-butane oxidation, Combust. Sci. Tech. 65 (1989) 207–230.
[4] P. Dagaut, M. Reuillon, J.C. Boettner, M. Cathonnet, Kerosene combustion at pressures up to 40 atm: experimental study and detailed chemical kinetic modeling, Symp. (Int.) Combust. 25 (1994) 919–926.
[5] C.J. Pope, J.A. Miller, Exploring old and new benzene formation pathways in low-pressure premixed flames of aliphatic fuels, Proc. Combust. Inst. 28 (2000) 1519–1527.
[6] J.A. Miller, C.F. Melius, Kinetic and thermodynamic issues in the formation of aromatic compounds in flames of aliphatic fuels, Combust. Flame 91 (1992) 21–39.
[7] R.P. Lindstedt, G. Skevis, Chemistry of acetylene flames, Combust. Sci. Tech. 125 (1997) 73–137.
[8] V. Detilleux, J. Vandooren, Experimental study and kinetic modeling of benzene oxidation in one-dimensional laminar premixed low-pressure flames, Combust. Explos. Shock Waves 45 (2009) 392–403.
[9] T. Faravelli, A. Goldaniga, L. Zappella, E. Ranzi, P. Dagaut, M. Cathonnet, An experimental and kinetic modeling study of propyne and allene oxidation, Proc. Combust. Inst. 28 (2000) 2601–2608.
[10] J.A. Miller, Theory and modeling in combustion chemistry, Symp. (Int.) Combust. 26 (1996) 461–480.
[11] H.J. Curran, J. Simmie, P. Dagaut, D. Voisin, M. Cathonnet, The ignition and oxidation of allene and propyne experiments and kinetic modelling, Symp. (Int.) Combust. 26 (1996) 613–620.
[12] R. Fournet, J.C. Bauge, F. Battin-Leclerc, Experimental and modelling of oxidation of acetylene, propyne, allene and 1,2-butadiene, Int. J. Chem. Kinet. 25 (1999) 361–379.
[13] A. Lifshitz, M. Frenklach, A. Burcat, Pyrolysis of allene and propyne behind reflected shocks, J. Phys. Chem. 80 (1976) 2437–2443.
[14] T. Kakumoto, T. Ushirogouchi, K. Saito, A. Imamura, Isomerization of allene ↔ propyne in shock waves and ab initio calculations, J. Phys. Chem. 91 (1987) 183–189.
[15] C.H. Wu, R.D. Kern, Shock tube study of allene pyrolysis, J. Phys. Chem. 91 (1987) 6291–6296.
[16] Y. Hidaka, T. Nakamura, A. Miyauchi, T. Shiraishi, H. Kawano, Thermal decomposition of propyne and allene in shock waves, Int. J. Chem. kinet. 21 (1989) 643–666.
[17] J.H. Kiefer, P.S. Mudipalli, S.S. Sidhu, R.D. Kern, B.S. Jursic, K. Xie, H. Chen, Unimolecular dissociation in allene and propyne: the effect of isomerization on the low-pressure rate, J. Phys. Chem. A 101 (1997) 4057–4071.
[18] J.F. Pauwels, J.V. Volponi, J.A. Miller, The oxidation of allene in a low-pressure H_2/O_2/Ar-C_3H_4 flame, Combust. Sci. Tech. 110–111 (1995) 249–276.
[19] J.A. Miller, J.V. Volponi, J.F. Pauwels, The effect of allene addition on the structure of a rich C_2H_2/O_2/Ar flame, Combust. Flame 105 (1996) 451–461.
[20] M.E. Law, T. Carriere, P.R. Westmoreland, Allene addition to a fuel-lean ethylene flat flame, Proc. Combust. Inst. 30 (2007) 1353–1361.
[21] H.A. Gueniche, P.A. Glaude, G. Dayma, R. Fournet, F. Battin-Leclerc, Rich methane premixed lamina flames doped with light unsaturated hydrocarbons I. allene and propyne, Combust. Flame 146 (2006) 620–634.
[22] N. Hansen, J.A. Miller., C.A. Taatjes, J. Wang, T.A. Cool, M.E. Law, P.R. Westmoreland, Photoionization mass spectrometric studies and modelling of fuel-rich allene and propyne flames, Proc. Combust. Inst. 31 (2007) 1157–1164.
[23] N. Hansen, J.A. Miller, P.R. Westmoreland, T. Kasper, K. Kohse-Hoinghaus, J. Wang, T.A. Cool, Isomer-specific combustion chemistry in allene and propyne flames, Combust. Flame 156 (2009) 2153–2164.
[24] P. Dagaut, M. Cathonnet, B. Aboussi, J.C. Boettner, Allene oxidation in jet-stirred reactor: a kinetic modelling study, J. Chem. Phys. 87 (1990) 1159–1172.
[25] S. Panigrahy, J.H. Liang, S.S. Nagaraja, G. Kim, S.S. Vasu, S. Dong, G. Kukkadapu, W.J. Pitz, H.J. Curran, A comprehensive experimental and improved kinetic modelling study on the pyrolysis and oxidation of propyne, Proc. Combust. Inst. 38 (1) (2021) 479–488.
[26] H. Nakamura, D. Darcy, M. Mehl, W.K.Metcalfe C.J.Tobin, W.J. Pitz, C.K. Westbrook, H.J. Curran, An experimental and modeling study of shock tube and rapid compression machine ignition of n-butylbenzene/air mixtures, Combust. Flame 161 (2014) 49–64.
[27] S.M. Burke, U. Burke, R. McDonagh, O. Mathieu, I. Osorio, C. Keesee, A. Morones, E.L. Petersen, W.J. Wang, T.A. DeVerter, M.A. Oehlschlaeger, B. Rhodes, R.K. Hanson, D.F. Davidson, B.W. Weber, C.J. Sung, J. Santner, Y.G. Ju, F.M. Haas, F.L. Dryer, E.N. Volkov, E.J.K. Nilsson, A.A. Konnov, M. Alrefae, F. Khaled, A. Farooq, P. Dirrenberger, P.A. Glaude, F. Battin-Leclerc, H.J. Curran, An experimental and modeling study of propene oxidation.Part 2: ignition delaytime and flame speed measurements, Combust. Flame 162 (2015) 296–314.
[28] Y. Li, C.W. Zhou, H.J. Curran, An extensive experimental and modeling study of 1-butene oxidation, Combust. Flame 181 (2017) 198–213.
[29] C. Morley, Gaseq, version 0.76, (2004).
[30] D. Darcy, C.J. Tobin, K. Yasunaga, J.M. Simmie, J. Würmel, W.K. Metcalfe, T. Niass, S.S. Ahmed, C.K. Westbrook, H.J. Curran, A high pressure shock tube study of n-propylbenzene oxidation and its comparison with n-butylbenzene, Combust. Flame 159 (2012) 2219–2232.
[31] L. Brett, Ph.D. Thesis, National University of Ireland, Galway, 1999.
[32] L. Brett, J. MacNamara, P. Musch, J.M. Simmie, Simulation of methane autoignition in a rapid compression machine with creviced pistons, Combust. Flame 124 (2001) 326–329.
[33] S.M. Gallagher, H.J. Curran, W.K. Metcalfe, D. Healy, J.M. Simmie, G. Bourque, A rapid compression machine study of the oxidation of propane in the negative temperature coefficient regime, Combust. Flame 153 (2008) 316–333.
[34] J. Würmel, J.M. Simmie, H.J. Curran, Studying of the chemistry of HCCI in a rapid compression machines, Int. J. Veh. Des. 44 (2007) 84–106.
[35] G. Kim, B. Almansour, S. Park, A.C. Terracciano, K. Zhang, S. Wagnon, W.J. Pitz, S.S. Vasu, Laminar burning velocities of high-performance fuels relevant to the Co-Optima initiative, SAE International Journal of Advances and Current Practices in Mobility 1 (2019) No. 2019-01-0571 1139-1147.
[36] B. Almansour, G. Kim, S. Vasu, The effect of diluent gases on high-pressure laminar burning velocity measurements of an advanced biofuel ketone, SAE Int. J. Fuels Lubr. 11 (4) (2018) 273–286.
[37] B. Almansour, S. Alawadhi, S. Vasu, Laminar burning velocity measurements in dipk-an advanced biofuel, SAE Int. J. Fuels Lubr. 10 (2) (2017) 432–441.
[38] Z. Chen, M.P. Burke, Y. Ju, Effects of compression and stretch on the determination of laminar flame speeds using propagating spherical flames, Combust. Theor. Model. 13 (2) (2009) 343–364.
[39] C. Xiouris, T. Ye, J. Jayachandran, F.N. Egolfopoulos, Laminar flame speeds under engine-relevant conditions: uncertainty quantification and minimization in spherically expanding flame experiments, Combust. Flame. 163 (2016) 270–283.
[40] C.-.W. Zhou, Y. Li, U. Burke, C. Banyon, K.P. Somers, S. Khan, J.W. Hargis, T. Sikes, E.L. Petersen, M. Alabbad, A. Farooq, Y. Pan, Y. Zhang, Z. Huang, J. Lopez, Z. Loparo, S.S. Vasu, H.J. Curran, An experimental and chemical kinetic modeling study of 1,3-butadiene combustion: ignition delay time and laminar flame speed measurements, Combust. Flame 197 (2018) 423–438.
[41] E. Goos, A. Burcat, B. Ruscic, Ideal gas thermochemical database with updates from active thermochemical tables, 2016, http://garfield.chem.elte.hu/Burcat/burcat.html
[42] X. Chen, C.F. Goldsmith, A theoretical and computational analysis of the methyl-vinyl + O_2 reaction and its effects on propene combustion, J. Phys. Chem. A 121 (48) (2017) 9173–9184.
[43] J.A. Miller, S.J. Klippenstein, From the multiple-well master equation to phenomenological rate coefficients: reactions on a C_3H_4 potential energy surface, J. Phys. Chem. A 107 (2003) 2680–2692.
[44] T. Faravelli, A. Goldaniga, L. Zappella, E. Ranzi, P. Dagaut, M. Cathonnet, An experimental and kinetic modeling study of propyne and allene oxidation, Proc. Combust. Inst. 28 (2000) 2601–2608.
[45] S.G. Davis, C.K. Law, H. Wang, An experimental and kinetic modelling study of propyne oxidation, Symp. (Int.) Combust. 27 (1998) 305–312.
[46] N. Hansen, J.A. Miller, C.A. Taatjes, J. Wang, T.A. Cool, M.E. Law, P.R. Westmoreland, Photoionization mass spectrometric studies and modeling of fuel-rich allene and propyne flames, Proc. Combust. Inst. 31 (2007) 1157–1164.
48 CHEMKIN-Pro 15131Reaction design, San Diego, 2013.
[48] J.A. Miller, J.P. Senosiain, S.J. Klippenstein, Y. Georgievskii, Reactions over multiple, interconnected potential wells: unimolecular and bimolecular reactions on a C_3H_5 potential, J. Phys. Chem. A 112 (2008) 9429–9438.
[49] J. Zador, J.A. Miller, Adventures on the C_3H_5O potential energy surface: OH + propyne, OH + allene and related reactions, Proc. Combust. Inst. 35 (2015) 181–188.
[50] T.L. Nguyen, J. Peeters, L. Vereecken, Quantum chemical and statistical rate study of the reaction of O (3P) with allene: O-addition and H-abstraction channels, J. Phys. Chem. A 110 (2006) 12166–12176.
[51] I. Gimondi, C. Cavallotti, G. Vanuzzo, N. Balucani, P. Casavecchia, Reaction dynamics of O (3P)+ propyne: II. Primary products, branching ratios, and role of intersystem crossing from ab initio coupled triplet/singlet potential energy surfaces and statistical calculations, J. Phys. Chem. A 120 (27) (2016) 4619–4633.
[52] J.G. Lopez, C.T. Rasmussen, H. Hashemi, M.U. Alzueta, Y. Gao, P. Marshall, C.F. Goldsmith, P. Glarborg, Experimental and kinetic modeling study of C_2H_2 oxidation at high pressure, Int. J. Chem. Kinet. 48 (11) (2016) 724–738.
[53] S.J. Klippenstein, J.A. Miller, A.W. Jasper, Kinetics of propargyl radical dissociation, J. Phys. Chem. A 119 (2015) 7780–7791.
[54] G. Vanuzzo, N. Balucani, F. Leonori, D. Stranges, S. Falcinelli, A. Bergeat, P. Casavecchia, I. Gimondi, C. Cavallotti, Isomer-specific chemistry in the propyne and allene reactions with oxygen atoms: CH_3CH+ CO versus CH_2CH_2+ CO products, J. Phys. Chem. Lett. 7 (2016) 1010–1015.
[55] G. Kukkadapu, S.W. Wagnon, W.J. Pitz, N. Hansen, Identification of the molecular-weight growth reaction network in counterflow flames of the

C_3H_4 isomers allene and propyne, Proc. Combust. Inst. 38 (1) (2021) 1477–1485.
[56] B. Ruscic and D.H. Bross, Active thermochemical tables (ATcT) values based on ver. 1.122 of the thermochemical network (2016); available at ATcT.anl.gov.
[57] Yu-Ran. Luo, Handbook of bond dissociation energies in organic compounds, CRC press, 2002.
[58] J.C. Lizardo-Huerta, B. Sirjean, R. Bounaceur, R. Fournet, Intramolecular effects on the kinetics of unimolecular reactions of β-HOROO$^{\cdot}$ and HOQ$^{\cdot}$OOH radicals, PCCP 18 (2016) 12231–12251.
[59] xxx 2021 https://bde.ml.nrel.gov/
[60] C.F. Goldsmith, W.H. Green, S.J. Klippenstein, Role of O2+QOOH in low-temperature ignition of propane. 1. Temperature and pressure dependent rate coefficients, J. Phys. Chem. A 116 (2012) 3325–3346.
[61] Y. Georgievskii, J.A. Miller, M.P. Burke, S.J. Klippenstein, Reformulation and solution of the master equation for multiple-well chemical reactions, J. Phys. Chem. A 117 (2013) 12146–12154.
[62] X. You, Y. Chi, T. He, Theoretical analysis of the effect of C=C double bonds on the low-temperature reactivity of alkenylperoxy radicals, J. Phys. Chem. A 120 (2016) 5969–5978.